博士論文

X-ray Selected Narrow-Line Active Galactic Nuclei in the COSMOS Field: Nature of Optically Dull Active Galactic Nuclei

(コスモス領域における X 線で選択した狭輝線活動銀河核: 可視光において活動銀河核の特徴の無い活動銀河核の性質)

Itsna Khoirul Fitriana
(イツナ　コイルル　フィトリアナ)

令和３年

X-ray Selected Narrow-Line Active Galactic Nuclei in the COSMOS Field: Nature of Optically Dull Active Galactic Nuclei

Itsna Khoirul Fitriana

A thesis submitted for the degree of Doctor of Philosophy in Astronomy

Graduate School of Science

Tohoku University

2021

Abstract

X-ray emission detection in a galaxy is one of the efficient tools for selecting Active Galactic Nuclei (AGNs). However, many X-ray-selected AGNs are not easily selected as AGNs by their optical emission. These galaxies, so-called optically dull (OD) AGNs, are fascinating since their X-ray emission is bright even though the AGN signature in the optical regime is absent. In a deep multiwavelength survey over 2 deg^2 of Cosmic Evolution Survey (COSMOS) field, we have looked for the OD AGNs using photometric, spectroscopic, and X-ray data. We identified 407 non-broad line sources as AGNs using X-ray selection up to redshift of $z \sim 1.5$. However, we only continue with 310 sources to be further inspected in the optical spectrum. We inspected the spectra to check for any AGN signature in their optical emission lines: [Ne V] forbidden emission line, Mass Excitation diagram (MEx), color excitation diagram (TBT), and excess in [O II] emission line. Finally,we found 48 AGNs show AGN signatures in optical spectrum classified as NL AGN and 180 AGNs that did not show any AGN signature as OD AGN sample. The simple explanation of OD AGN's nature is due to a bright host galaxy that dilutes the AGN light or due to dust materials obscuring the AGN light. We found that the bright host galaxy dilution explains nearly 70% of our OD AGN sample. At the same time, the dust material obscuration is unlikely for the main reason. By estimating the Eddington ratio, we also found that 95/180 of our OD AGNs have a lower accretion rate of $(\lambda_{\mathrm{Edd}}) \lesssim 10^{-2}$ than the typical AGN value. We expected the lower accretion rate sources that suffer from neither host galaxy dilution nor obscuration to have Radiatively Inefficient Flow (RIAF) in their accretion disk. Finally, nine sources have been identified to be most likely host the RIAF disk.

Keyword: AGN – Narrow line – Optically dull

This thesis is composed of my original work, and contains no material previously published or written by another person except where due reference has been made in the text. I have clearly stated the contribution by others to jointly-authored works that I have included in my thesis.

I have clearly stated the contribution of others to my thesis as a whole, including statistical assistance, survey design, data analysis, significant technical procedures, professional editorial advice, financial support and any other original research work used or reported in my thesis. The content of my thesis is the result of work I have carried out since the commencement of my higher degree by research candidature and does not include a substantial part of work that has been submitted to qualify for the award of any other degree or diploma in any university or other tertiary institution. I have clearly stated which parts of my thesis, if any, have been submitted to qualify for another award.

I acknowledge that an electronic copy of my thesis must be lodged with the University Library and, subject to the policy and procedures of Tohoku University, the thesis be made available for research and study in accordance with the Copyright Act unless a period of embargo has been approved by the Dean of the Graduate School.

I acknowledge that copyright of all material contained in my thesis resides with the copyright holder(s) of that material. Where appropriate I have obtained copyright permission from the copyright holder to reproduce material in this thesis and have sought permission from co-authors for any jointly authored works included in the thesis.

Submitted manuscripts included in this thesis

1. **Fitriana, Itsna K.**, and Murayama, Takashi, X-ray Selected Narrow-Line Active Galactic Nuclei in the COSMOS Field: Nature of Optically Dull Active Galactic Nuclei, submitted to *Publication of the Astronomical Society of Japan (PASJ)* on 16th December 2021.

Contents

List of Figures

List of Tables

Chapter 1

Introduction

Most galaxies, particularly massive galaxies with stellar mass of $M_* \sim 10^{10}\ M_\odot - 10^{12}\ M_\odot$, host a supermassive black hole (SMBH) at their nucleus (Kormendy and Richstone, 1995). Essentially all SMBHs in massive galaxies are thought to experience the active growth of their SMBH, during which they are observed as active galactic nuclei (AGN) (Marconi et al., 2004). The AGN term is related to the compact region at the center of a galaxy that emits more radiation than the rest of the host galaxy. They are now believed to be powered by the accretion of mass onto SMBHs. As the gas accretes onto SMBH, the potential energy of the gas is converted to high luminosity radiation across the electromagnetic wavelengths, from radio to X-ray and up to γ-ray.

The optical spectra observation generally classifies AGNs as type 1, also known as broad line AGN (BL AGN), based on the presence of both broad and narrow emission lines, and type 2 or narrow line AGN (NL AGN) that only presents the narrow emission lines. The lack of a broad emission line of NL AGN is attributed to a dusty structure obscuring the central engine and the broad-line region (BLR). This model is well known as the traditional unification model introduced by Antonucci (1993). The standard AGN unified model has successfully used obscuration to explain the differences between BL AGN and NL AGN. In the straightforward interpretation of this model, all AGNs have the broad optical emission lines and strong UV/optical continua of BL AGNs, but along certain lines of sight, these features are obscured by a dusty obscuring structure a few parsecs from the black hole. This model is supported by the detection of polarised broad emission lines of NL AGN (Antonucci and Miller (1985)) and the detection of a high X-ray column density in most of them. It supports the idea that BL AGN and NL AGN are intrinsically the same, but the lack of a broad emission line and weaker optical continuum of NL AGNs were attributed to obscuration by torus structure covering both the central engine and BLR.

However, a simple unified model has a limit in explaining the whole observations of AGN

since it is based solely on geometric obscuration. There is observational evidence of objects showing opposite X-ray and optical classification. First, some BL AGNs shows significant absorption in the X-ray band (Maiolino et al. (2001), Brusa et al. (2003), Merloni et al. (2013)). A possible explanation is that the dust to gas ratio in these sources is lower than the Galactic value (Maiolino et al. (2003))). Thus, such an obscuring material primarily made of gas and with very little dust will be opaque in the soft X-rays but transparent at optical wavelengths permitting the observation of a broad emission line.

On the contrary, unobscured NL AGNs have been reported observationally (Hawkins (2004), Brightman and Nandra (2008), Trump et al. (2011a), Merloni et al. (2013), Pons et al. (2016)). By definition, the NL AGN should show a hidden BLR if we observe through a spectropolarimetry observation. Otherwise, many NL AGNs show no broad emission line even in very deep spectropolarimetric observation. Moreover, deep X-ray surveys also have revealed "optically dull" (OD) AGNs (Comastri et al. (2002); Merloni et al. (2013); Trump et al. (2009)), which emit bright X-ray emission but lack of optical AGN signature.

The nature of OD AGNs could be explained by some hypothesis such as dilution from the prominent host galaxies' light (Moran et al. (2002); Trump et al. (2009); Pons et al. (2016)) or obscuration by dusty material near the central engine or beyond the host galaxies(Civano et al. (2007); Rigby et al. (2006)). The other exciting nature is an explanation that the OD AGNs could have a different intrinsic structure that caused a lower accretion rate than typical AGN (Yuan and Narayan (2004); Trump et al. (2011a)).

A complete census of AGN is an important goal to understand the vital role of the SMBH in the galaxy evolution. However, these inconsistencies between optical and X-ray selection of AGN are a significant obstacle. Mainly, X-ray selection of AGN will be highly efficient compared to the optical selection, which might be suffered by high obscuration of the intervening material and dilution of light from the host galaxy. This shows the limitation in finding and characterizing OD AGN.

Rigby et al. (2006) studied the OD AGN earlier with limited observational data and could only find 22 OD AGNs. This small sample in redshift $0.5 < z < 0.8$ characterized OD AGN as an obscured AGN that tends to be hosted by edge-on galaxies. This result is against the later studies by Trump et al. (2009) that stated their sample of 48 OD AGNs in redshift up to $z \sim 1$ did not affect by host galaxies obscuration. This study found that the primary nature of OD AGNs is due to host galaxy dilution. However, Pons et al. (2016) found different results for more local galaxies in redshift up to $z \sim 0.4$ that the optical dullness is mainly due to the intrinsic weakness of AGN. Previous studies' different conclusions regarding the OD AGN's properties and nature motivated us to explore the OD AGN in recent observational data.

Cosmic Evolution Survey (COSMOS) is a promising project to identify OD AGNs and characterize their properties in a larger sample. This is because the project provides multiwave-

length datasets that had been observed using most of the major space-based and ground-based telescopes (Civano et al. (2007)). By using the recent catalog in X-ray and optic, we could draw a more significant sample up to a redshift of $z \sim 1.5$. The availability of this extensive dataset benefits us in studying OD AGN in more complete ways. Furthermore, we also do not only use the traditional BPT diagram to find the absence of AGN signatures in optics but also some recent diagnostic tools for distant sources.

Apart from the census of OD AGN, that may represent a significant missed of the AGN population, the mismatch between X-ray and optical observation suggests a question regarding the viewing-angle orientation as the only parameter to distinguish AGN's type (Padovani et al., 2017) (as explained in the traditional unified model). Therefore, the study of OD AGN is essential for a better understanding of the AGN's physical structure as well as the accretion physics as one of the hypotheses of optical dullness comes from the intrinsic weakness of nuclei that could give a different structure of accretion disk than the normal AGN.

Observations suggest a lower accretion rates of $L/L_{\rm Edd} \lesssim 0.01$ could keep the formation of BLR away in AGNs (Trump et al. (2011a)). In the absence of BLR formation, it becomes understandable that OD AGNs give no AGN signature in the optical regime. Narayan et al. (2012) also suggests that the normal thin disk (Shakura and Sunyaev (1973)) at a lower accretion rate could be truncating into a geometrically thick and optically thin Radiatively Inefficient Accretion Flow (RIAF) disk at lower radii near the SMBH. Such an object is predicted to have weak UV/optical emission and lack strong emission lines. This property is usually observed among the local galaxies of weak low-luminosity AGNs (Nemmen et al. (2006); Narayan et al. (2012)) and some found in X-ray bright OD AGNs (Yuan and Narayan (2004); Trump et al. (2011a)).

The quasar representing powerful intrinsic nuclei show decreasing numbers rapidly below a redshift $z \sim 2$. Since Quasars are essentially non-existent in the local universe, $z \sim 0$, Yi (1996) suggested that quasars may switch their accretion from standard thin disk to RIAF at $1 \lesssim z \lesssim 2$. This provides the natural explanation of the decreasing number of QUASAR in smaller redshift since the RIAF disks were observed to be significantly less luminous and thus much more difficult to detect. By combining with present RIAF sources in a local universe, our sample of OD AGNs in moderate redshift could test the theory and give a complete picture of accretion disk evolution.

This work presents the sample of X-ray AGNs in the COSMOS field with further spectral type analysis as NL AGNs and OD AGNs. We aim to find a larger sample of OD AGN using novel diagnostic tools. A better understanding of OD AGN also can be seen with the properties different from normal AGN that here we use a sample of NL AGN. Finally, we test some hypotheses of optical dullness to obtain the possible nature of OD AGN in our sample. This test also expects sources with lower accretion rates that are likely to host a RIAF disk. We will use

these sources, as RIAF candidates, in future work to study the accretion disk evolution.

This thesis is organized as follows. Chapter 2 describes the selection of the X-ray AGN sample. Chapter 3 describes the optical spectrum classification to find the AGN signature among the X-ray AGN and to find the OD AGN. In Chapter 4 we present the difference of NL AGNs and OD AGNs in host galaxy properties and X-ray properties. Chapter 5 discusses the possible reasons for the optical dullness of our sample. Chapter 6, we discuss our OD AGN that is most likely to host RIAF with a previous study of RIAF sources. Finally, we summarize our work in Chapter 7. We adopt a cosmology with $h = 0.70, \Omega_M = 0.3$, and $\Omega_\Lambda = 0.7$ throughout.

Chapter 2

X-ray AGN Sample and Data

To study the OD AGNs, multiwavelength data is necessary to give us better understanding of these objects. For that purpose, we used a set of photometric and spectroscopic data from the Cosmic Evolution Survey (COSMOS) project. The main datasets of COSMOS field cover a 2 square degree region around the center (J2000:150.1192, 2.2058), but some datasets extend significantly beyond this region (Scoville et al., 2007). The field has been observed at all accessible wavelengths with most of the major space-based (Hubble, Spitzer, GALEX, XMM, Chandra, Herschel, NuStar) and ground-based telescopes (Subaru, Keck, Very Large Array (VLA), European Southern Observatory Very Large Telescope (ESO-VLT), United Kingdom Infrared Telescope (UKIRT), The National Optical Astronomical Observatory (NOAO) and Blanco telescopes, the Canada France Hawaii Telescope (CFHT), and others). The COSMOS project has already pioneered the study of galactic structures at intermediate to high redshifts and the evolution of the galaxy and AGN populations which is a big help for a researcher to study the universe better.

The available data from X-ray, UV, optical/IR, mid-infrared, mm/submillimeter to radio with extremely high sensitivity imaging and spectroscopy is required to study the OD AGN completely. We adopted the X-ray data from Chandra COSMOS (C-COSMOS) legacy catalog

Catalog Name	**Wavelength**	I_{AB}	**Data used**	**Reference**
C-COSMOS legacy	X-ray (0.5-10 keV)	$\leq$24.6	X-ray properties	Marchesi et al. (2016)
COSMOS2015	multiwavelength	$\leq$25-26	Photometry, SED fitting products	Laigle et al. (2016)
Z-COSMOS	5500 – 9659 Å	$\leq$25	Optical spectrum	Lilly et al. (2007)
Deimos10K	5500 – 9800 Å	$\leq$23	Optical spectrum	Hasinger et al. (2018)
ZEST Morphology	$\sim$ 4000 – 6700 Å	$\leq$24	Morphological poperties	Scarlata et al. (2007)

Table 2.1: Catalog in COSMOS project that were used in this work

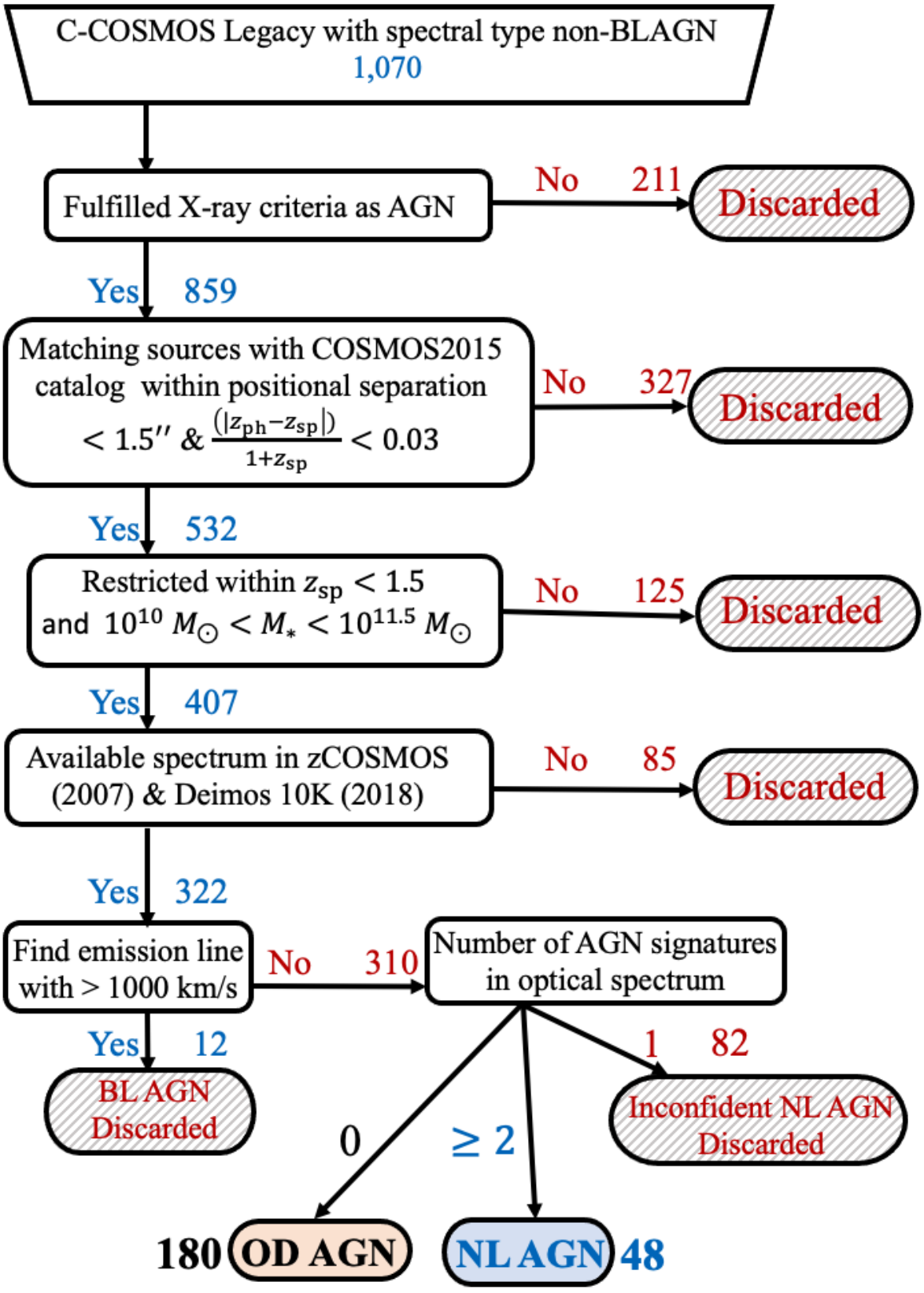

Figure 2.1: Flowchart

A flow chart of our sample selection scheme. See text for details

(Marchesi et al., 2016), the photometry and spectral energy distribution (SED) products in UV, optical, and near-infrared wavelength from the COSMOS2015 catalog (Laigle et al., 2016), the optical spectrum data from zCOSMOS and DEIMOS10K catalog, and the optical morphological catalog from the Zurich Estimator of Structural Types (ZEST) catalog (Scarlata et al., 2007). We summarize the COSMOS catalogs used in this work in Table 2.1. Meanwhile the whole process of our AG data selection is summarized in a flowchart in Figure 2.1.

2.1 X-ray AGN selection

The C-COSMOS catalog by Marchesi et al. (2016) contains 4016 X-ray sources down to flux limits of 2.2×10^{-16} erg cm^{-2} s^{-1}, 1.5×10^{-16} erg cm^{-2} s^{-1}, and 8.9×10^{-16} erg cm^{-2} s^{-1} in energy bands of $0.5-2$ keV, $2-10$ keV, and $0.5-10$ keV, respectively. Furthermore, We used available X-ray properties in the catalog: the X-ray luminosity, hardness ratio (HR), hydrogen column density ($N_{\rm H}$).

Besides the X-ray properties, this catalog also presented the counterpart optical and near infrared data. So therefore, there are 1770 sources available with reliable spectroscopic redshifts ($z_{\rm sp}$) and spectral type information under COSMOS project collaboration. The spectral type classified 632 sources as BL AGNs as showing at least one broad emission line ($FWHM > 2000$ km s^{-1}) in their optical spectra. We do not further use these BL AGNs in our following work. Meanwhile, other 1070 sources were classified as non-broad-line AGNs (non-BL AGNs) with only a narrow emission line or no emission line. Note that the "non-BL AGN" class includes "non-AGN" galaxies such as star-forming (SF) galaxies since the C-COSMOS catalog did not further separate them from NL AGNs. Instead of emission line classification of optical spectra, we adopted criteria following Trump et al. (2009) to eliminate SF galaxies among the non-BL AGNs,

$$L_{0.5-10\rm keV} > 3 \times 10^{42} \rm erg\ s^{-1}, \tag{2.1}$$

or

$$-1 \leq X/O \leq 1, \tag{2.2}$$

where

$$X/O = \log f_X/f_O = \log f_{0.5-2\rm keV} + i_{\rm AB}/2.5 + 5.352,$$

where $f_{0.5-2\rm keV}$ is in the unit of erg cm^{-2} s^{-1} while $i_{\rm AB}$ is in the unit of mag. The luminosity limit in equation 2.1 sets these constraints on X-ray luminosity in local SF galaxies. Meanwhile, equation 2.2 is known as traditional "X-ray AGN locus" of Maccacaro et al. (1998) which show typical X-ray to optical ratio value of AGN. These criteria are reliable in selecting AGN

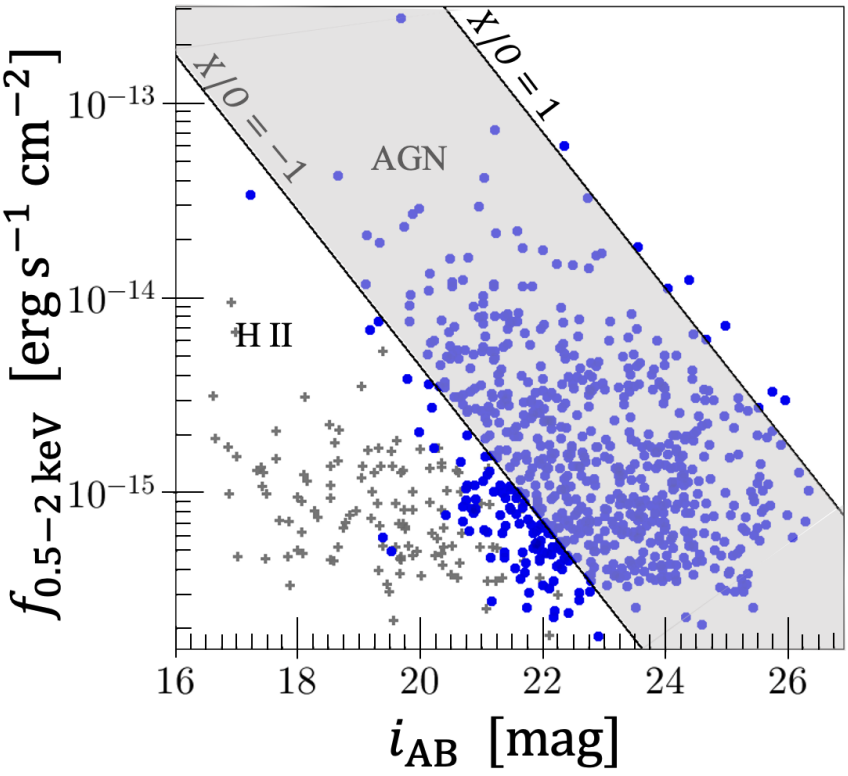

Figure 2.2: Soft X-ray flux vs. i-band magnitude, for non-BL AGN sample. The grey shaded region defines the AGN locus with an optical X-ray ratio (X/O) between -1 and 1. Blue dots are the selected X-ray AGN, and the grey cross symbol is the remaining source. There are only three sources that lower X-ray luminosity but are located in the AGN locus.

without contamination of powerful SF galaxies (i.e., X-ray binary systems, ultra-luminous X-ray sources), with $L_X \sim 10^{39} - 10^{41}$ erg s^{-1}. The sources were defined as X-ray AGN if they satisfy at least one of the two criteria above. Finally, we found 859 galaxies satisfied the criteria as X-ray AGNs.

In Fig. 2.2, blue dots indicate X-ray AGNs that satisfy at least one criterion of equation 2.1 or equation 2.2. The AGN locus shows the criterion 2.2 in the grey shaded area between the two black solid lines ($-1 \leq X/O \leq 1$). Both criteria show mutually supportive results as many as 567 sources (66%). Meanwhile, only 2% of the sources which only meet the second criterion. Having two criteria to select the AGN will give us more sources to be included in our sample.

2.2 Redshift and stellar mass restriction

After selecting the 859 X-ray AGNs, we matched them with sources in the COSMOS 2015 catalog. The catalog presents newer version of the precised photometric redshift (z_{ph}) and contain more than half-million sources in the field of COSMOS survey. The catalog also derived the absolute magnitudes, stellar mass, star formation rates, and other valuable properties of host galaxies using the best fitting of 30-band photometry data SED . These photometric

data sample, derived from many hundreds of hours of telescope time in different surveys: UV survey of *GALEX*(Zamojski et al. (2007)), optical 20 bands using Suprome-Cam instrument of Subaru (Taniguchi et al. (2007);Taniguchi et al. (2015)), Near-Infrared survey with the VIRCAM instrument as part of the UltraVISTA survey (McCracken et al. (2012)), and Mid-IR by *Spitzer* cycle 2 COSMOS survey (Sanders et al. (2007)). These are a key ingredient to discover the precise $z_{\rm ph}$.

Matching process of our sample with COSMOS2015 catalog was performed both with (1) coincidence of the central positions in the C-COSMOS catalog and the COSMOS 2015 catalog within $1.5''$, and (2) coincidence of the spectral redshifts ($z_{\rm sp}$) in the C-COSMOS catalog and the photometric redshifts ($z_{\rm ph}$) in the COSMOS 2015 catalog within $|z_{\rm sp}-z_{\rm ph}|/(1+z_{\rm sp})<0.03$. Resulting number of the sample is 532.

Next, we restricted our sample in the range of redshift ($z<1.5$) and stellar mass ($10^{10}\,M_{\odot}<M_*<10^{11.5}\,M_{\odot}$) to constrain and let us draw a fair sample and reject the bias analysis due to the observation limit. The redshift range is also required for finding the emission lines that will be use in the optical AGN selection. These redshift and stellar mass limits reduced the number of samples to 407.

Chapter 3

Optical Spectrum Classification

We used galaxy optical spectra available from the z-COSMOS catalog (Lilly et al., 2007) and DEIMOS 10K spectroscopic survey catalog (Hasinger et al., 2018). Both catalogs were being undertaken in the COSMOS field, giving us a good cross-matched with the C-COSMOS legacy catalog. Z-COSMOS is a large-redshift survey that uses 600 hours of observation with the VIMOS spectrograph on the 8 m VLT. The survey is designed to characterize COSMOS galaxies' environments from the 100 kpc scales of galaxy groups to the 100 Mpc scale of the cosmic web and produce diagnostic information on galaxies and active galactic nuclei. In the z-COSMOS catalog, we found the spectrum of 149 galaxies among the 407 X-ray AGNs remaining in the previous selection. Meanwhile, Hasinger et al. (2018) presented the first comprehensive spectroscopic observations with the Deep Imaging Multi-Object Spectrograph (DEIMOS) on the Keck II telescope in the wavelength range of $\sim 5500-9800$ Å. field of view (FOV) of DEIMOS is approximately 16×4 arcmin^2, which allows placement of slit masks in the field for multi-object spectroscopy of $\sim 60-100$ objects. The DEIMOS 10K spectroscopic catalog provides a higher resolution (R$\sim 2000-2700$) than the zCOSMOS catalog. With deeper magnitude limits, $i_{AB} < 23.5-25$ mag, we expect to obtain a larger sample for our study. Of our X-ray AGNs, the optical spectrums of 197 galaxies were found in the Deimos 10K catalog. Furthermore, the same restrictions in the matching process for C-COSMOS legacy and COSMOS2015 catalogs were used in the matching process for each catalog used in this research, including here with the spectrum data catalogs. In total, we found 322 spectrum galaxies from both spectroscopy catalogs, with 24 sources overlapping in both catalogs.

We further inspected the available spectra of 322 galaxies to check the existence of AGN signatures in them. We used the latest version of the `SPECUTILS` (Astropy Collaboration et al., 2018) package in `PYTHON` for analysing our optical spectrum. We obtain the emission line properties by fitting an emission line spectra with a single Gaussian model. We only take the emission line with a signal-to-noise ratio of $S/N > 3$. Thus, we believe that we draw a

trustworthy sample classification. At first, we looked whether broad emission lines were still present and the galaxies which presented the emission lines broader than 1000 km s^{-1}. This threshold rejects all bonafide broad-line objects and reduces conventional narrow-line Seyfert 1 (NLS1) galaxies contamination (Caccianiga et al., 2007). The NLS1, which is part of BL AGN, can have line widths narrower than FWHM$<$ 2000 km s^{-1}. It results in they were not classified as broad line AGN in the C-COSMOS catalog. We found 12 galaxies with broad lines larger than 1000 km s^{-1} in their spectra and discarded them from our sample.

The most commonly used diagnostic tools to separate AGN and SF population by optical emission is the BPT diagram (Baldwin et al., 1981), which use the [O III]λ5007/Hβ and [NII]λ6584/Hα line ratios. Since the redshift of our sample is mostly $z \gtrsim 0.3$, popular emission lines used in the BPT analysis (i.e. [N II]λ6584 and Hα) were shifted out of the optical spectral range. Therefore, alternative indicators have been proposed to find the AGN signature in optical spectrum. Particularly, we searched for the [Ne V] forbidden emission line at $\lambda = 3426$ Å , which is a good indicator of AGN activity (Heckman and Best (2014); Pouliasis et al. (2020); Padovani et al. (2017)). We also adopted the Mass Excitation diagram (MEx) that uses the [O III]λ5007/Hβ versus M_* (Juneau et al. (2011); Juneau et al. (2014)), the color excitation diagram (TBT) that use the [Ne III]λ3869/[O II]λ3727 versus $(g-z)$ rest-frame color (Trouille et al., 2011). In addition, we used the novel method by Tanaka (2012), that uses [O II] luminosity to separate AGN contribution from star-forming galaxies.

We have applied these four diagnostic tools based on the emission line and galaxy properties to look for any galaxy with no signature in all methods. We marked them as OD AGN. Meanwhile, the sources classified as AGN by at least two diagnostic tools classified as NL AGN. Unconfident NL AGNs showed an AGN signature by only one diagnostic tool and we did not include them as NL AGN due to a lack of confidence.

3.1 [Ne V] emitters

[Ne V]λ3426 has the same physical origin as the [O III]λ5007, arising from photoionized gas in the narrow line region (NLR). This line arises well outside the region of the heaviest obscuration (Padovani et al. (2017)). The ionizing potential of [Ne V] is 97 eV, which may only come from high energy sources as the NLR of AGN. Mignoli et al. (2013) who identified NL AGNs that emit [Ne V], then compared them to the AGNs which selected by X-ray selection, concluded that the AGN that emits [Ne V] were able to identify low-luminosity and heavily obscured AGNs. Among our X-ray AGN sample, there are 47 X-ray AGNs that clearly show [Ne V] emission lines in their spectrum.

Figure 3.1 show the example in our sample that shows an [NeV] emission. The line was clear compared to the noise. Besides the [NeV] signature, the sources could give other signatures with

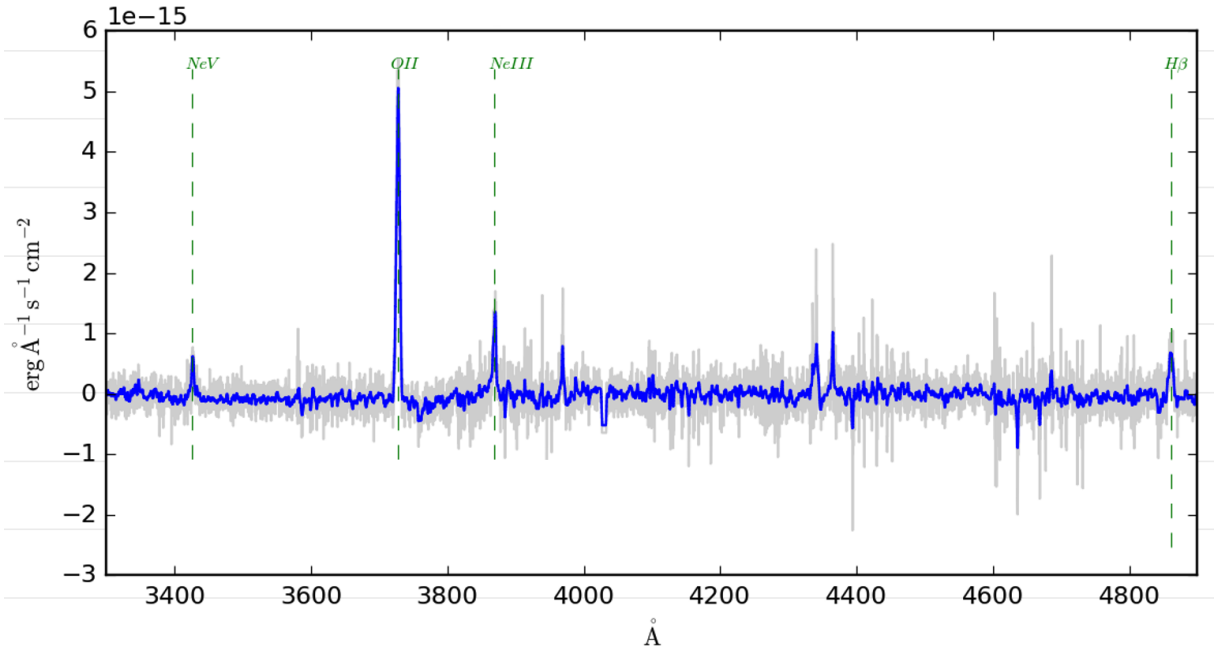

Figure 3.1: [Ne V] emission in NL AGN spectra

other methods explained in the following subsections. In this source spectra, we can spot the high [O II] emission and also [Ne III] emission, which also possibly can indicate the existence of AGN in the center region.

3.2 MEx diagram

The Mass-Excitation (MEx) diagnostic tool has been proposed by Juneau et al. (2011). Instead of using the [N II]λ6584/Hα line ratio as in the classic BPT diagram, the MEx diagram uses the galaxy's stellar mass as a surrogate. The MEx technique successfully distinguishes the emission line originating from SF or AGN, possibly dealing with composite galaxies, which lie in the part of the diagram between the AGN and SF region.

We used the revised two demarcation line as written in Juneau et al. (2014) (see equation (1) and (2) in their paper). As shown in Figure 3.2, we found that 24 sources are classified as AGN by MEx optical diagram method among 26 sources with reliable measurements of [O III]λ5007/Hβ and stellar mass. The remaining two sources are located precisely in the SF region, which gives us no sources placed as composite galaxies.

3.3 TBT diagram

Trouille et al. (2011) has been constructed the diagram with sample using in the Sloan Digital Sky Survey (SDSS) that is based on the $g-z$ rest-frame optical color ($^0(g-z)$) as a function of

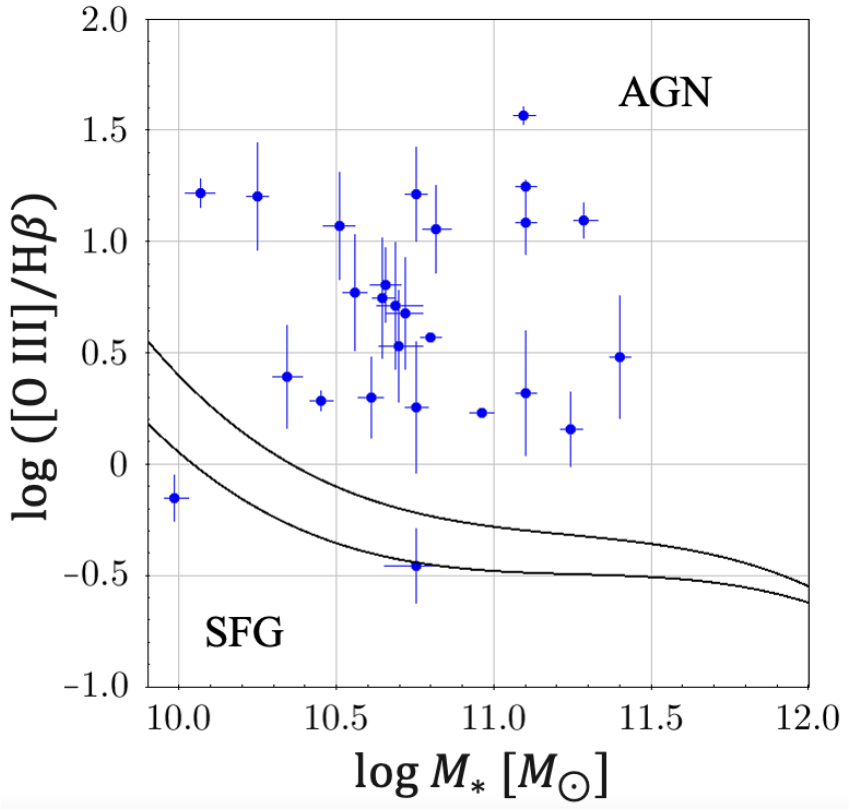

Figure 3.2: MEx diagram for the X-ray AGNs. The solid black line show demarcation lines between the MEx-AGN, the-composites, and the MEx-SF.

the ratio of [Ne III]λ3869 and [O II]λ3727. The optical classification can be extended up to a redshift of $z \sim$1.4 using only these two emission lines. Moreover, this diagram has the advantage of being little affected by reddening because the [Ne III]λ3869 and [O II]λ3727 are relatively close in wavelength. There is only one criterion for selecting AGN as follows:

$$^{0}(g-z) > -1.2 \times \log([\text{Ne III}]\lambda 3869/[\text{O II}]\lambda 3727) - 0.4. \quad (3.1)$$

By this criterion, our sample shows that 54 sources fall inside the AGN area as shown in Figure 3.3. In comparison, only four sources lie in the star-forming region. This method can be applied to a large fraction of our samples due to the emission line availability in wide redshift range. Besides it is pretty easy to use, this method gives significant overlap with the other diagnostic tools.

3.4 [O II] emission excess

This technique was developed by Tanaka (2012) to study their low-luminosity AGN sample in the SDSS archive data. Tanaka (2012) demonstrated a comparison between observed luminosity

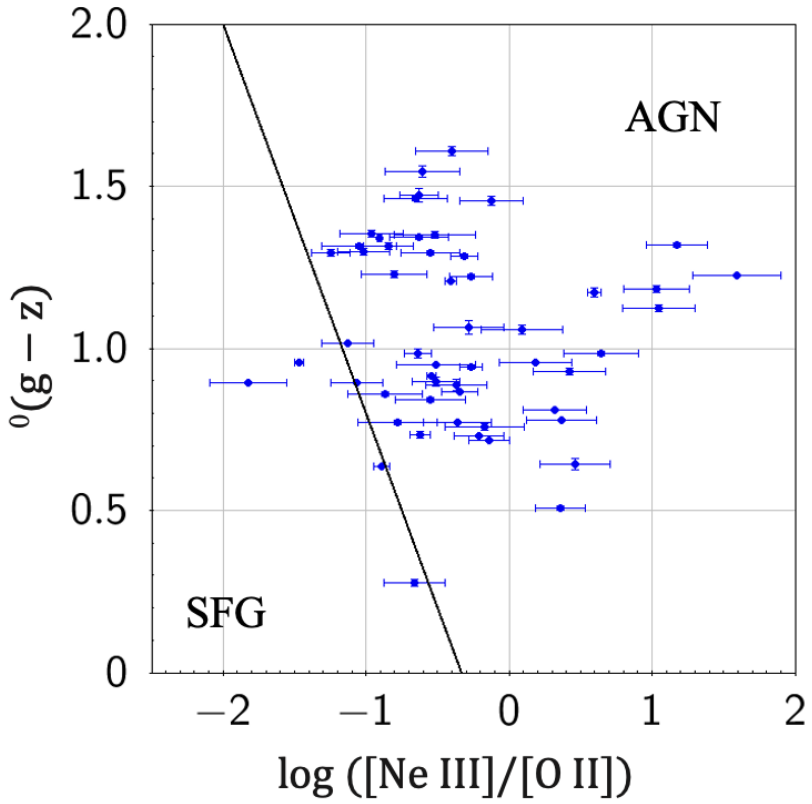

Figure 3.3: TBT diagram for the X-ray AGNs. The solid black line separated the star-forming galaxies from the AGNs.

with that attributed to star formation to distinguish whether a galaxy host an AGN or not. It can be applied at high redshift without making any prior assumptions about host galaxy properties.

The original "Oxygen-excess method" uses the total emission line that comes from [O II]λ3727 and [O III]λ5007. Even so, we use only the [O II]λ3727 line regarding the distant objects in our sample mostly showed only the [O II]λ3727 emission line.

The [O II]λ3727 emission can arise from the star-forming region (SF region), and the NLR in a galaxy hosts an AGN. In other words, the observed emission is a combination of SF and AGN, or we can write as,

$$L_{[\mathrm{O\ II}],\mathrm{obs}} = L_{[\mathrm{O\ II}],\mathrm{SF}} + L_{[\mathrm{O\ II}],\mathrm{AGN}} \tag{3.2}$$

where $L_{[\mathrm{O\ II}],\mathrm{obs}}$ is the [O II] luminosity measured directly from the observation, $L_{[\mathrm{O\ II}],\mathrm{SF}}$ and $L[\mathrm{O\ II}]_{\mathrm{AGN}}$ are the contribution of [O II] emission coming from the host galaxy and AGN respectively.

Fig. 3.4 shows the comparison between the [O II] luminosity that is directly measured from the optical spectrum ($L_{[\mathrm{O\ II}],\mathrm{obs}}$) and the [O II] luminosity estimated from the SFR ($L_{[\mathrm{O\ II}],\mathrm{SF}}$). Here, Tanaka (2012) show a systematic offset between the observed luminosity and the SF estimation luminosity for SF galaxies which is shown in a black dashed line as $\log L_{[\mathrm{O\ II}],\mathrm{obs}} = \log L_{[\mathrm{O\ II}],\mathrm{SF}} + 0.16$ with a scatter of $\sigma = 0.23$. Then, the original definition of the AGN selection

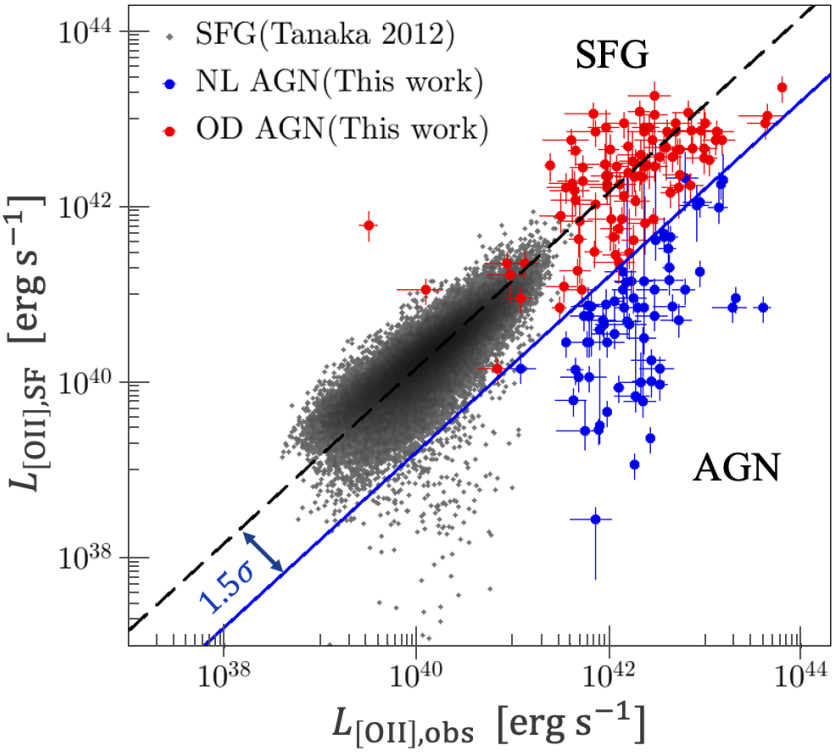

Figure 3.4: The relation between [O II]λ3727 luminosity, which measured directly from the observed spectrum, and the one that derived from the star formation rate (SFR). The region above the solid blue line shows the typical emission line arising from the SF region. In contrast, the region under the blue line shows the excess of [O II]λ3727emission line in the galaxy, probably coming from the AGN at the most. The grey dots are the distribution of Star-Forming Galaxies (SFG) in Tanaka (2012) work.

by this method is shown by the excess of $L_{[\mathrm{O\ II}],\mathrm{obs}}$ to the $L_{[\mathrm{O\ II}],\mathrm{SF}}$ by $> 1.5\sigma$ (shown by the blue solid line) after considering the offset. Thus, we can define the AGN sample as those with,

$$\log \frac{L_{[\mathrm{O\ II}],\mathrm{obs}}}{L_{[\mathrm{O\ II}],\mathrm{SF}}} > 0.16, \tag{3.3}$$

The $L_{[\mathrm{O\ II}],\mathrm{obs}}$ in this work were directly measured from the available spectrum, which had been calibrated to the photometry flux. Meanwhile, the $L_{[\mathrm{O\ II}],\mathrm{SF}}$ is calculated from SFR equation following Kennicutt (1998) as described below,

$$L[\mathrm{O\ II}](10^{41}\mathrm{erg\ s^{-1}}) = \frac{SFR(\mathrm{M_\odot\ yr^{-1}})}{(1.4 \pm 0.4)} \tag{3.4}$$

After all, we found 69 sources laid above the solid blue line in Fig. 3.4 and thus they do not have an AGN excess in [O II] emission line. The [O II] emission observed in these galaxies is typically coming from their star-forming region of host galaxies.

Sample	Optical spectra	Total	z_{sp}	$\log M_*$	$\log SFR$	$\log L_{0.5-10\mathrm{keV}}$
OD AGN	no AGN signatures	180	$0.34-1.488$	10.78 ± 0.3	1.01 ± 0.96	43.18 ± 0.41
NL AGN	≥ 2 AGN signatures	48	$0.511-1.478$	10.82 ± 0.32	0.48 ± 1.1	43.37 ± 0.42
Discarded for the following analysis						
unconf NL AGN	1 AGN signature	82	$0.317-1.449$	10.78 ± 0.33	0.75 ± 1.12	43.28 ± 0.48
BL AGN	FWHM ≥ 1000 km s^{-1}	12	$0.133-1.323$	10.44 ± 0.25	1.69 ± 1.16	43.66 ± 0.61

Table 3.1: The terms used to define various type of AGN in this work

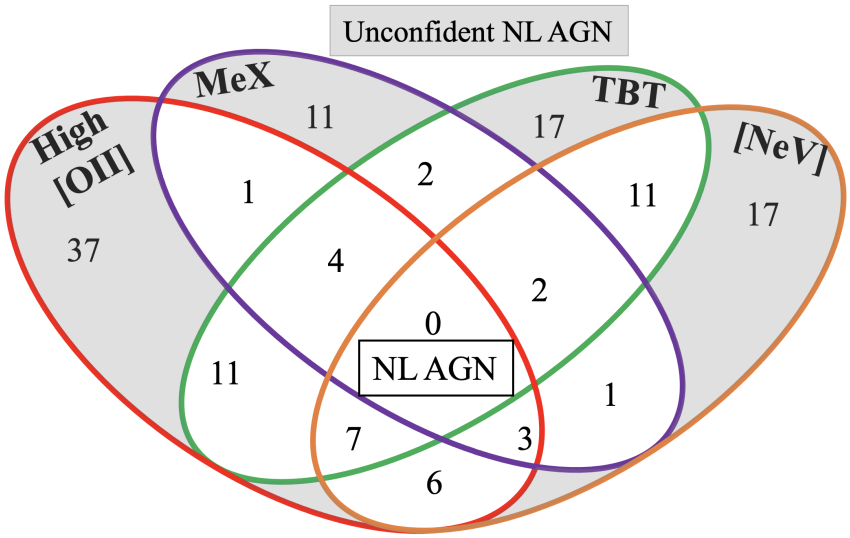

Figure 3.5: The result by optical classification method in Section 3. The NL AGNs are described inside the blue line, which shows that sources are selected as AGN by more than one diagnostic tool. Otherwise, the darker color shape shows the unconfident NL AGN selected by only one diagnostic tool.

3.5 Final sample of OD AGNs and NL AGNs

Our optical spectrum selection for NL AGNs in section 3 is shown by Venn diagram as in Figure 3.5 and Table 3.2. Some methods are consistent; one source was concluded as NL AGN by more than one method. Due to the redshift range in our sample, it is only natural that the OII emission line is the most observed in our sources.

An object is defined as AGN if a source had been shown AGN signatures by more than one method (the white area), then 48 (15%) sources were selected as NL AGN. The term NL AGN in the subsequent analysis refers to this sample definition. Meanwhile, we also found sources selected as AGN by only one diagnostic tool classified as unconfident sources (illustrated in the greyed area). We found 82 (15%) sources to be unconfident NL AGNs. These unconfident NL AGNs will be discarded in the following work. Finally, we could draw our main target, OD AGN, as the source that could not show AGN signature by any diagnostic tools.

Table 3.1 show that the redshift range of the final sample. The NL AGN are distributed in the redshift range of $0.511 \leq z_{sp} \leq 1.478$ while the OD AGNs ranges in the $0.34 \leq z_{sp} \leq 1.488$. The fact that our X-ray AGN yields in the higher redshift even for OD AGN, which was not

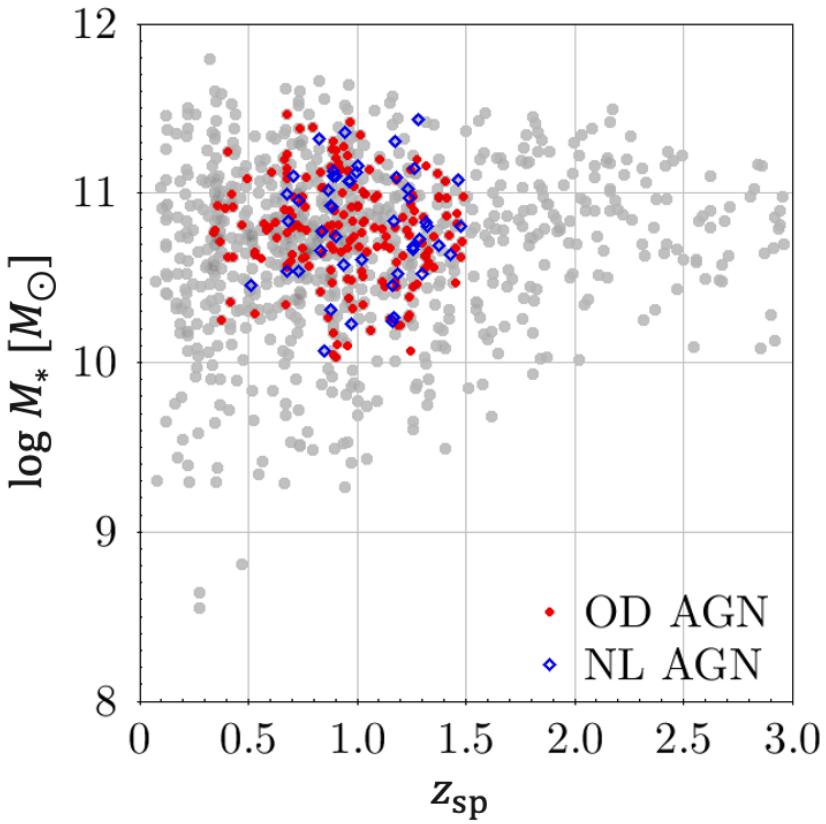

Figure 3.6: The stellar mass of galaxies vs. redshift. The OD AGN (red dots) and NL AGN (blue diamond) are able to be found in the mass range 10.0 $M_\odot \leq M_* \leq$ 11.5 $M_\odot$ and reshift up to z$\leq$1.5. The grey dots are the X-ray sources in C-COSMOS catalog type as non-broad line AGN (which might be contain narrow line AGN and or normal galaxies)

Table 3.2: The optical classification result from Chapter 3

Classification	total number	[NeV]	MeX AGN	TBT AGN	[O II] Excess
NL AGN (unconfident)	17	✓			
NL AGN	1	✓	✓		
NL AGN	2	✓	✓	✓	
NL AGN	3	✓	✓		✓
NL AGN	11	✓		✓	
NL AGN	7	✓		✓	✓
NL AGN	6	✓			✓
NL AGN (unconfident)	11		✓		
NL AGN	2		✓	✓	
NL AGN	4		✓	✓	✓
NL AGN	1		✓		✓
NL AGN (unconfident)	17			✓	
NL AGN	11			✓	✓
NL AGN (unconfident)	37				✓
OD AGN	180				

showing any AGN signature in optical, is most likely due to the spectroscopic data availability. There is also not much difference in the stellar mass distribution, which gives an unbias sample regarding the galaxy's properties. However, we could still find that most OD AGNs give a higher SFR and lower X-ray luminosity than NL AGN.

Chapter 4

Results

As illustrated in Fig. 2.1, we finally obtained 48 NL AGNs and 180 OD AGNs samples. Due to the redshift range in our sample, [O II]λ3727 emission line is the most observed in our sources, therefore, we compare the [O II]λ3727 luminosity for the NL AGN and OD AGN samples in this section. There is only one source in the NL AGN sample that does not show [O II]λ3727 emission line, and the remaining 47 NL AGN are [O II]λ3727 emitters. Meanwhile, there are 97 OD AGNs that show [O II]λ3727 emission line.

Besides the emission line comparison, we also present comparison of host galaxy properties between NL AGN and OD AGN samples. We use the axial ratios of the host galaxies from the COSMOS morphological catalog, which is obtained from the Zurich Estimator of Structural Types (ZEST; Scarlata et al. (2007)) catalog.

In order to ensure that our result is not suffered from observation limit, we already selected our sample in the specific range of stellar mass and redshift, which is shown in Figure 3.6.

4.1 Comparison of [O II] luminosity and hard X-ray luminosity

The X-ray emission is the unmistakable signature of AGN activity. In our selection process, we use the high luminosity constraint to select AGN using the total X-ray luminosity ($L_{0.5-10\mathrm{keV}}$). It is enough evidence that our sample is not strongly contaminated with star-forming galaxies (which has typical X-ray luminosity $\sim 10^{39}$ erg s^{-1} (Mineo et al., 2011)). Therefore, the X-ray emission here can be representative of AGN activity.

In the subsection 3.4, we already distinguished the sources that have typical [O II]λ3727 emission coming from star-forming galaxies as OD AGN and the sources which showed an excess as the NL AGN. Therefore, the origin of [O II]λ3727 is different for both samples. Since there is no excess of [O II]λ3727 emission observed in the spectral data compared to the

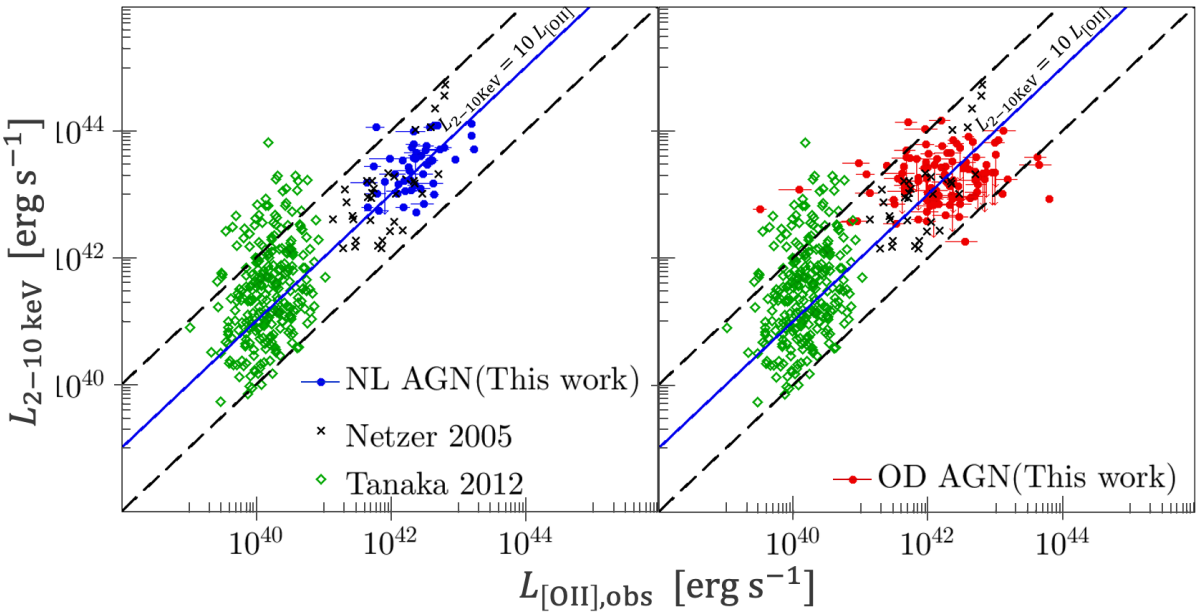

Figure 4.1: The relation between observed [O II]λ3727 luminosity and hard X-ray luminosity (2-10 keV). Both panels show our sample (left for NL AGN in blue dots, right for OD AGN in red dots) compared to the previous study by Netzer et al. (2006) in the black cross and Tanaka (2012) in the green diamond. The solid line shows the ratio of hard X-ray to [O II]λ3727 luminosity equal to 10, while dashed line shows the ratio value of 1 (lower dashed line) and 100 (upper dashed line).

SFR estimation, the [O II]λ3727 of OD AGN sources is concluded to become only from its host galaxy. Meanwhile, the excess of [O II]λ3727 emission observed in the NL AGN is the unmistakable evidence that a certain fraction of [O II]λ3727 emission of NL AGN sources was also coming from NLR as an AGN contribution.

Some previous studies already show a good relation between the [O III]λ5007 line and X-ray emission of AGN (Zakamska et al. (2003); Zakamska et al. (2004); Netzer et al. (2006)). Thereupon, Zakamska et al. (2003) presented a perfect linear relationship between [O II]λ3727 line and the [O III]λ5007 line in their AGN sample. It leads to an expectation that the [O II]λ3727 line will also show a good relation with hard X-ray (2-10 keV) as shown in the [O III]λ5007 line. The expected relation is clearly shown in our works, joining with the previous study that showed in Fig. 4.1.

The blue dots of NL AGNs in the left panel of Fig. 4.1 show neatly gathered around the solid line, which represents the ratio of X-ray luminosity and [O II]λ3727 luminosity equals to ten. It is in good agreement with a previous study by Netzer et al. (2006) in the black crosses, and Tanaka (2012) in the green diamonds. The sample that was used by Tanaka (2012) are drawn from SDSS and classified as AGN using a BPT diagram. Their sample concentrates in more local universe than our sample. They are lower luminous than ours. Meanwhile, Netzer et al. (2006) which used higher redshift sample, defined their sample as NL AGN based on the X-ray

criteria in the luminosity and column density ($L_{2-10\mathrm{keV}} > 10^{42}$ erg s^{-1} and $N_{\mathrm{H}} > 10^{22}\mathrm{cm}^{-2}$). Only two sources show an upper limit in X-ray luminosity which are shown with the blue down arrows. However, still these sources show the typical value of $L_{2-10\mathrm{keV}}/L_{[\mathrm{O\ II}]} = 10$.

Meanwhile, the OD AGNs, shown in the red circles in the right panel of Fig. 4.1, distribute more scattered than NL AGNs. By this weak correlation among the OD AGNs, it gives us a proof that the majority of [O II]λ3727 emission were not coming from AGN. Instead, it is more likely to come from the star-forming regions of the host galaxies.

However, the OD AGN sample is still found to have a value consistent with the typical NL AGNs, which means that their host galaxy is basically bright enough to dilute their AGN optical signature. In opposite, the OD AGNs that situate above the black dashed line in Fig. 4.1 which has higher X-ray luminosity of $L_{2-10\mathrm{keV}}/L_{[\mathrm{O\ II}]} > 100$ are considered to has a nucleus (represent by X-ray luminosity) that is brighter than the nuclei in the typical NL AGN. The dilution scenario is difficult to explain since their AGN's light should be outshined the host galaxies' light. It leads us to find that a physical effect might depress their optical emission while remaining bright in X-ray.

4.2 Host galaxy properties

We use secure morphological information of axial ratios and half light radii in F814W of HST ACS for 47 NL AGNs, and 177 OD AGNs obtained from the ZEST catalog (Scarlata et al., 2007). For very compact objects, the instrumental point-spread function (PSF) could affect the axial ratio calculation. The limiting size/magnitude in which the effects of the PSF become important could make the preference of the morphological galaxy tends to be elliptical type. Despite, Scarlata et al. (2007) stated that the ZEST catalog could measure the morphological parameters of the COSMOS sources without being affected by PSF convolution unless for sources with half-light radii of $R_{1/2} < 0.17''$. The number of sources in our sample with $R_{1/2} < 0.17''$ are only four NL AGNs and four OD AGNs, which means that PSF unlikely affect our result.

We present the distribution of axial ratio for OD AGNs (red line histogram) along with NL AGNs (blue shaded histogram) in Fig. 4.2. Rigby et al. (2006) shows that X-rays select AGNs in host galaxies with wide range of axial ratio, but only AGNs that show optical emission (optically active) are observed in the most face-on host galaxies. It supports the idea that extranuclear dust in the host galaxy plays an important role in hiding the emission lines of OD AGNs. They compare the morphologies of 22 OD AGNs and 9 optically active AGNs that contains of BL AGN and NL AGN at $0.5 < z < 0.8$. Their OD AGNs distribute in the axial ratio range of $0.26 \leq b/a \leq 0.89$, nwhile all their optically active AGNs have $b/a > 0.79$. In contrast with our sample, the OD AGNs and NL AGN have nearly similar ranges of axis ratio b/a, with the OD AGN mean value $b/a = 0.66 \pm 0.19$ and the NL AGN mean $b/a = 0.71 \pm 0.13$. The mean value

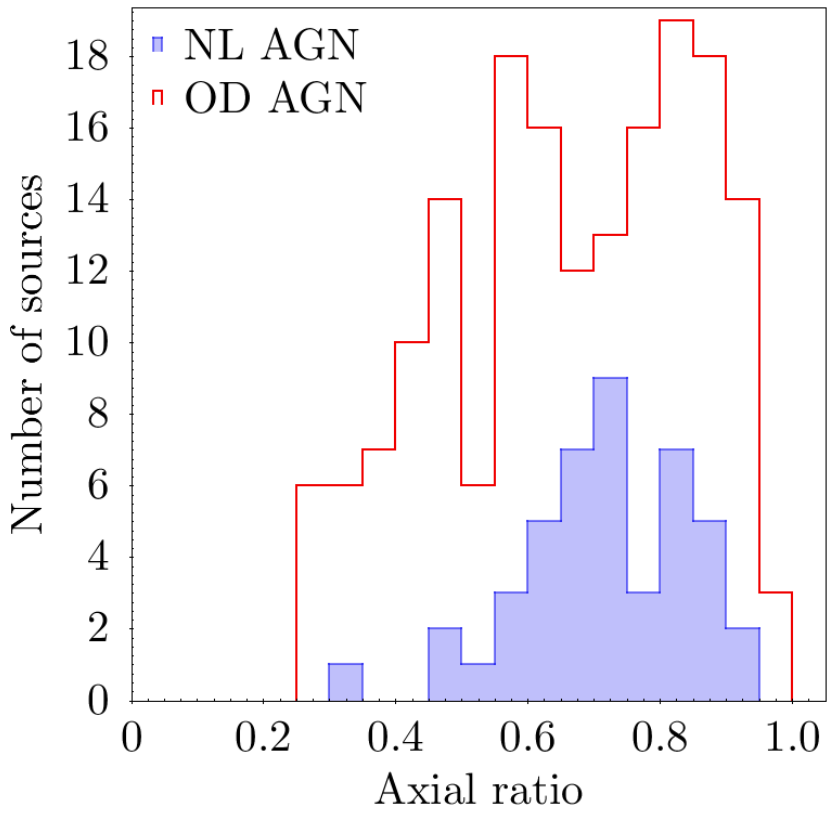

Figure 4.2: Axial ratio (b/a) histogram for the OD AGN (red line) NL AGN (shaded blue) sample. The axial ratio of OD AGNs and NL AGNs in our sample show similar range with no preference for specific value of inclination angle.

is slightly different from the sample of Trump et al. (2009) (OD AGN $b/a = 0.56 \pm 0.2$, NL AGN $b/a = 0.56 \pm 0.18$), which used a lower redshift sample ($z \lesssim 1.0$).The NL AGNs in our sample which are slightly higher redshift are most possibly shows the face-on preferences. However, it is not shown in our NL AGNs or even in NL AGNs sample of Trump et al. (2009) that Rigby et al. (2006) claims for their 'optically active' AGN sample tend to be face-on preference. We agree with Trump et al. (2009) that the difference comes from their sample definitions containing type 1 BL AGNs. In contrast, our sample only contains the NL AGNs. The morphological fits to BL AGN host galaxy could suffer from systematical errors due to bright nuclei. In particular, a BL AGN host could have an incorrectly high b/a value. In the end, we conclude that the edge-on host is not the leading cause of the optical dullness among our OD AGN sample.

Chapter 5

Nature of Optically Dull AGNs

In this Chapter, we will explore possible reasons for the optical dullness of our OD AGNs. Since we already examined host obscuration in section 4.2, we present three principal natures for this dullness of OD AGNs, with some critical differences concerning the scenarios presented in previous studies:

1. *X-ray Obscuration*. Intrinsic X-ray emissions heavily attenuated by dust, rendering these X-ray AGNs unclassifiable by any optical methods in Section 3 (Comastri et al. (2002); Civano et al. (2007)).

2. *Star formation dilution*. Optical spectra taken by slit spectroscopy are contaminated by the emission from star-forming regions that changes the resulting emission line observed otherwise as a star-forming or normal galaxy (Moran et al. (2002); Pons et al. (2016); Agostino and Salim (2019)).

3. *Low-accretion rate AGN.* The AGN is suspected of hosting a radiatively inefficient accretion flow (RIAF) which cannot adequately heat the NLR (Yuan and Narayan (2004); Trump et al. (2011a)).

5.1 X-ray obscuration

One common explanation of optical dullness in OD AGN is obscuration by material near the central engine. Comastri et al. (2002) suggested that OD AGNs have precisely a similar physical engine as BL AGN or NL AGN, but with additional gas and dust's obscuration covering a few parsecs from the nuclear source. This scenario could provide the necessary obscuration for blocking the ionizing radiation to excite in the NLR. However, obscuring the optical emission while remaining the X-ray emission bright would require extreme gas to dust ratios. It is due to

the most OD AGNs were observed relatively unabsorbed with the hydrogen column density of $N_{\rm H} < 10^{22}$ cm^{-2} (Severgnini et al. (2003)).

To consider a necessary obscuration of the central engine, Civano et al. (2007) proposed the obscuration caused by spherical Compton-thick gas cloud covering $\sim 4\pi$ of the central region. This type of cloud's geometry will prevent the ionizing photons from escaping from the nuclear source and producing narrow line emission in the NLR. Here we used X-ray hardness ratio (HR) for estimating the obscuration level.

The HR statistically indicates the amount of absorption by assuming the primary power-law domination and the similar spectral index in all sources. The X-ray spectrum of an AGN with a higher intrinsic absorption level is much harder than an unabsorbed one because the absorber deferentially attenuates the soft X-ray emission. The HR value from the C-COSMOS legacy catalog was defined as

$$HR = \frac{H - S}{H + S} \tag{5.1}$$

H is the net count in the X-ray energy band of $2-10$ keV and S is obtained in the X-ray energy band of $0.5-2$ keV. The relation between hardness ratio and the hydrogen column density $N_{\rm H}$ was also calculated in the C-COSMOS legacy catalog at all redshift. Fig. 5.1 is shown the relation of HR and $N_{\rm H}$ along with the redshift. There are three curves of different column density ($N_{\rm H} = 10^{22}$ cm^{-2}, 10^{23} cm^{-2}, and 10^{24} cm^{-2} from bottom to top respectively), obtained assuming a power-law spectrum with a photon index of $\Gamma = 1.8$. As shown in 5.1, there are no sources laid above the curve $N_{\rm H} = 10^{24}$ cm^{-2} which is the lower limit of the Compton thick cloud. It gives us evidence that the Compton thick cloud hypothesis could not explain our sample's optical dullness. Moreover, the X-ray emission will be significantly absorbed and scattered again in higher energy above 10 keV (outside the Chandra X-ray telescope observable energy range). It means that high obscuration by Compton clouds is not possible in our sample since our sample gives a bright X-ray emission lower than the 10 keV energy band.

Pons et al. (2016), who also used sample in the COSMOS field, tested the presence of Compton thick obscuration using a different method. They looked for the hard X-ray and [O III]λ5007 luminosity ratio ($L_{HX}/L_{[\rm O\ III]}$) of their sample sources which are smaller than 0.2 as a threshold of the Compton thick cloud obscuration existence. A high absorption level near nuclear will depress the X-ray luminosity, while NLR's [O III]λ5007 emission should be unaffected. In the end, they found all their sources lie above the Compton thick threshold ranging from 0.5 to 50. Therefore, it could be concluded if the X-ray obscuration is not the nature of their optical dullness sample, which agrees with our result.

Even though the high X-ray obscuration is not among our sample, the moderate absorption ($N_{\rm H} = 10^{22}$ cm^{-2} -10^{24} cm^{-2}) might be an additional nature of optical dullness to the diluted OD AGNs. As shown in Fig. 5.1, most sources located above the blue solid curve $N_{\rm H} = 10^{22}$

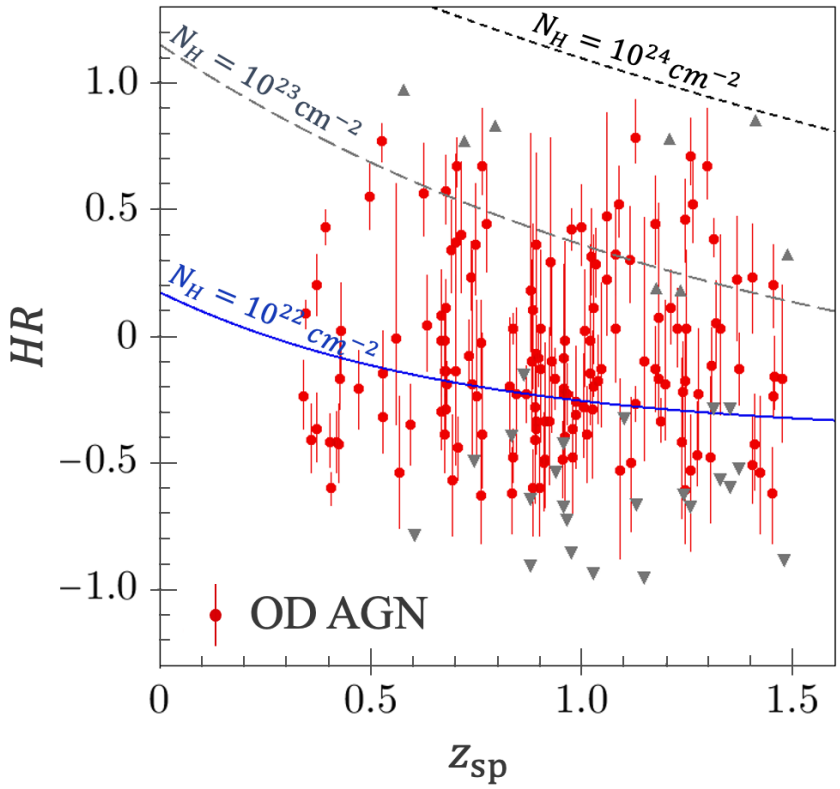

Figure 5.1: Hardness ratio (HR) relation with sectroscopic redshift (z_{sp}) for OD AGN sample in red dots symbol. The upper limit is shown in upside triangle while the lower limit is shown in downside triangle. Three curves of different column density (N_H) are plotted as comparison, obtained assuming a power-law spectrum with $\Gamma = 1.8$: (10^{22} cm^{-2} in solid blue line, 10^{23} cm^{-2} in grey long dashed line, 10^{24} cm^{-2} in black short dashed line)

cm^{-2} which is the typical limit to classify sources as NL AGN (moderately absorbed type) by X-ray emission. Meanwhile, we could not neglect the significant sources under the solid blue curve, a typical BL AGN value (unabsorbed type). We use the curve to separate our OD AGN sample as moderately absorbed (sources with column density of $N_H > 10^{22}$ cm^{-2}) and unabsorbed (sources with column density of $N_H < 10^{22}$ cm^{-2}) for the following analysis. By this definition, we found 103 sources as absorbed OD AGN and 77 sources as unabsorbed OD AGN (including 20 upper limit sources).

5.2 Star formation dilution

The other way to explain the nature of OD AGN's optical dullness is the dilution by the host galaxy to the nuclear emission. Dilution could happen due to the spectroscopic aperture reason. Moran et al. (2002) used a large spectroscopic aperture to demonstrate that not so few nearby NL AGNs are diluted by the SF light of their hosts. This scenario would come if the entire galaxy and occasionally even a nearby galaxy's companion were included in the spectroscopic slit.

By half-light radii in the ZEST morphological catalog, we compare the galaxy size with

the aperture size of the slit. Both z-COSMOS (Lilly et al., 2007) and Deimos 10K Hasinger et al. (2018) catalogs used in this study used the multi-slit spectrograph, that has a single slit size equal to $1'' \times 10''$. Let us only consider the slit width and neglect the slit length. We can see that 145 (80%) of our OD AGNs has a smaller half light radii than the spectroscopy aperture, which means that they were observed by including the entire galaxy. The remaining 35 (20%) OD AGN sources have a size larger than the slit width. Thus, it is understandable that many 'optically normal' AGNs could appear 'optically dull' when we observed the entire galaxy placed in the spectroscopic apertures.

Moran et al. (2002) found 60% of their sample appear optically dull due to larger observational aperture than the galaxy size and that fraction of Trump et al. (2009) was about 70%. Compared to their result, our sample shows a slightly higher fraction. It is possibly caused by our sample are taken at higher redshift up to $z \sim 1.5$, while others are in more local universe; Moran et al. (2002) use sample up to $z \lesssim 0.5$, and Trump et al. (2009) used sample up to $z \lesssim 1.0$. More distant galaxies will likely be captured within the entire galaxy and diluted more likely.

The dilution also can be considered by the host galaxy's light contributions compared to the AGN. As discussed in section 4.1, we found that the [O II] luminosity from NL AGN gives a good relation with hard X-ray. At the same time, OD AGN show more scatters in Fig. 3.4. It is shown that [O II] luminosity among our OD AGNs is likely coming from the SF region without any AGN contamination.

We introduce a parameter $R_{\text{HX-[O II]}}$ as the ratio of $L_{2-10\text{keV}}$ and $L_{\text{[O II]}}$ as written below,

$$R_{\text{HX-[O II]}} = \log \frac{L_{2-10\text{keV}}}{L_{\text{[O II]}}}. \tag{5.2}$$

This ratio estimates the AGN strength over the host galaxy among our OD AGN sample. Meanwhile, $R_{\text{HX-[O II]}}$ of NL AGN gives different meaning since there is an AGN contamination over the [O II] emission line. It causes the [O II] luminosity of NL AGN is not appropriate to be host galaxy's representative. However, the typical $R_{\text{HX-[O II]}}$ value of NL AGNs by this work as well as two previous studies could give us an estimation of AGN strength. Consequently, we could find the bright host galaxy that possibly dilutes the OD AGN's light if we compare $R_{\text{HX-[O II]}}$ of OD AGN with that of NL AGNs ($R_{\text{HX-[O II]}} < 2$).

Fig. 5.2 basically shows the dilution effects among our OD AGNs with comparing $R_{\text{HX-[O II]}}$ with half-light radii. The region under the horizontal line represents that the spectroscopic aperture is comparable to the size of host galaxy. We have found that the spectroscopic aperture dilutes 80% of our OD AGN sample. However, bright AGN might be suffering from this dilution scenario. Hereabouts, we also consider the AGN light compared to the host galaxy light, represented by the X-ray and [O II] luminosity ratio as $R_{\text{HX-[O II]}}$. Hence, We put the constrain in the x-axis equal to 2 ($L_{2-10\text{keV}} = 100 \times L_{\text{[O II]}}$) to state the AGN light that possibly overwhelm the galaxy light due to it is brighter than the typical NL AGNs.

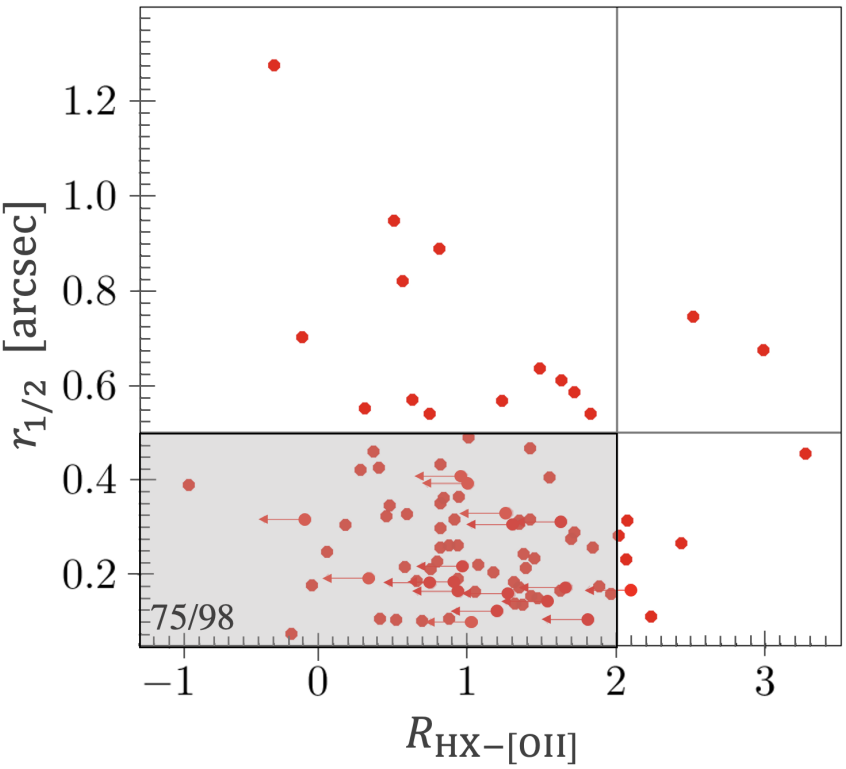

Figure 5.2: The $R_{\text{HX-[O II]}}$ as AGN domination over host galaxy vs. the half-light radii ($r_{1/2}$). The horizontal line represents the size of the spectroscopic aperture (slit size $\sim 1''$) while the vertical line represents the limit of the typical value of NL AGN's ($R_{\text{HX-[O II]}} = 2$).

The OD AGNs, which has $R_{\text{HX-[O II]}}$ value more than the vertical line in Fig. 5.2, should be brighter and could overshine the host galaxy. Thus, along with the additional effect of large observational aperture, we found 75 out of 98 ($\sim 75\%$) sources likely to be diluted by their host galaxies (shown in grey shaded area). Moreover, the sources with a $R_{\text{HX-[O II]}}$ value more than the vertical line ($R_{\text{HX-[O II]}} = 2$) and have a larger size ($r_{1/2} > 0.5''$) are unlikely to have a host galaxy's dilution to explain their optical dullness. It gives us an indication that there is another nature to their optical dullness.

5.3 Low accretion rate AGN

AGNs with low accretion rates are expected to be optically underluminous, with very weak or missing emission lines (Narayan et al., 1998). In this section, we will investigate the third reason for the optical dullness hypothesis by estimating the specific accretion rate using the Eddington ratio parameter $\lambda_{\text{Edd}} \equiv L_{\text{bol}}/L_{\text{Edd}}$. Here, L_{bol} will be estimated using the X-ray luminosity. In contrast, the Eddington luminosity is derived from the black hole mass.

Estimating BH masses for AGNs without broad emission lines requires secondary estimators. We use the well-studied correlation between BH and bulge mass of the host galaxy(Marconi and Hunt, 2003).

$$\log(M_{\rm BH}) = 8.12 + 1.06(M_{\rm bulge} - 10.9), \tag{5.3}$$

where $M_{\rm BH}$ is the blackhole mass and $M_{\rm bulge}$ is stellar mass of the bulge component in unit of $M_{\odot}$. More recent studies estimated the $M_{\rm BH}$ using the K-band luminosity relation (Graham (2007); Vika et al. (2011); Läsker et al. (2013)) instead of the stellar mass. We also tried the K-band luminosity relation in our sample and it still gives similar range of $M_{\rm BH}$. However, we prefer to keep our calculation using $M_{\rm BH} - M_{\rm bulge}$ relation which is systematically tighter relation than that the $M_{\rm BH} - L_{\rm K,bulge}$ relation, where $L_{\rm K,bulge}$ is the K-band luminosity of the host galaxy's bulge. It is expected if $L_{\rm bulge}$ correlates with $M_{\rm BH}$ because of its dependence on $M_{\rm bulge}$ through the stellar mass to light M/L ratio.

Furthermore, we combine the total galaxy's stellar mass from Laigle et al. (2016) with bulge fractions from morphological classification by ZEST catalog (Scarlata et al. (2007)) in order to determine the $M_{\rm bulge}$. We adopted a study by Lusso et al. (2012) which give a fraction of the bulge-to-total (B/T) based on the morphological type as well as the bulgeness level, which are presented in the ZEST catalog as follows :

1. elliptical :B/T=1,
2. bulge-dominated disc: B/T=0.75,
3. intermediate-bulge disc: B/T=0.5,
4. disc-dominated: B/T=0.25,

In the ZEST catalog, 142 OD AGNs and 34 NL AGNs are classified as one of the above types of morphology. Meanwhile, the remaining 38 OD AGNs and 14 NL AGNs are classified as irregular type or unable to determine. For these sources, we employed the M_* as $M_{\rm bulge}$ in the BH mass estimation ($B/T = 1$) and considered them as upper limit value (the open square symbol in Fig. 5.3).

We estimated the bolometric luminosity of AGN from the X-ray luminosity by applying a bolometric correction. We have used hard X-ray luminosity ($L_{2-10\rm keV}$), while those with the upper limit of hard X-ray, the soft X-ray luminosity ($L_{0.5-2\rm keV}$) was used. Assuming relations by Lusso et al. (2012), the bolometric corrections were derived as follow:

$$\log\left(\frac{L_{\rm bol}}{L_{2-10\rm keV}}\right) = 1.256 + 0.23\mathscr{L} + 0.05\mathscr{L}^2 - 0.001\mathscr{L}^3, \tag{5.4}$$

and

$$\log\left(\frac{L_{\rm bol}}{L_{0.5-2\rm keV}}\right) = 1.399 + 0.217\mathscr{L} + 0.009\mathscr{L}^2 - 0.010\mathscr{L}^3, \tag{5.5}$$

where $\mathscr{L} = \log L_{\rm bol} - 12$, and $L_{\rm bol}, L_{2-10\rm keV}, L_{0.5-2\rm keV}$ are in the unit of $L_{\odot}$. This bolometric correction are performed for NL AGN which assume the instrinsic nuclear luminosity are coming

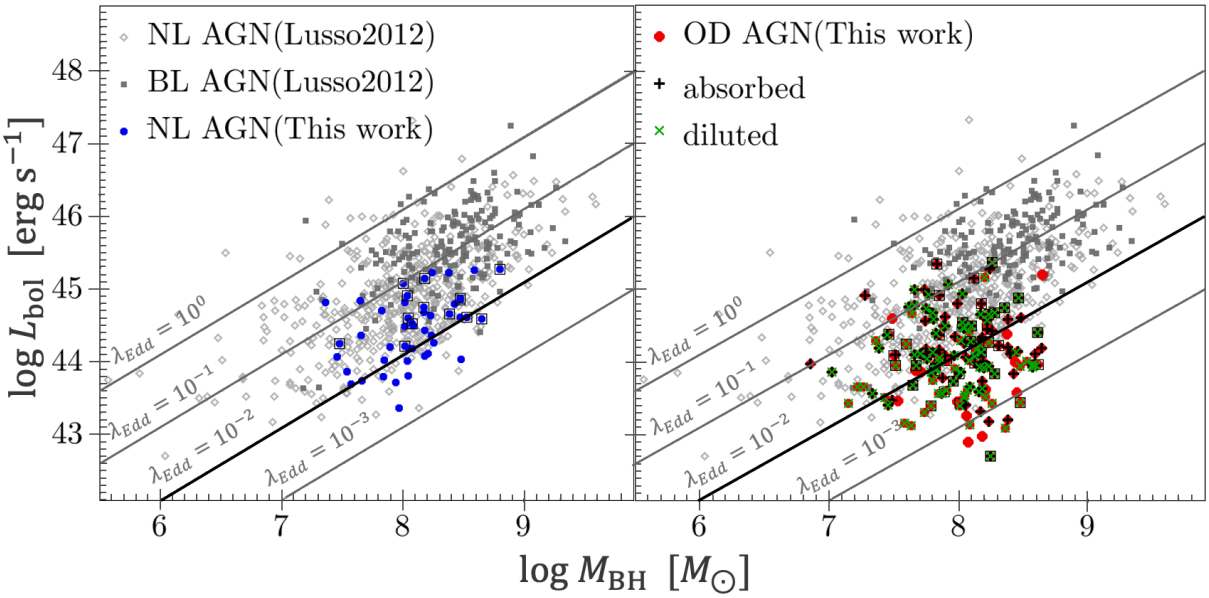

Figure 5.3: The diagram of BH mass (M_{BH}) vs bolometric luminosity (L_{bol}) for our works compare with Lusso et al. (2012) in grey diamonds and squares symbols. The NL AGN in this work show in blue dots (left panel) while the OD AGN show in the red dots (right panel). The diagonal line shows a similar value to the Eddington ratio ($\lambda_{Edd} = 10^0, 10^{-1}, 10^{-2}, 10^{-3}$, upper left to bottom right, respectively). The upper limit value of black hole masses is shown in the black square in both diagrams. There is also additional information for diluted and absorbed OD AGN in black plus and green cross symbol respectively.

from the IR and X-ray luminosities. The mid-IR luminosity is considered as an indirect probe of the accretion disc optical/UV luminosity.

In Fig. 5.3, the bolometric luminosities (L_{bol}) are plotted as a function of BH masses (M_{BH}) for OD AGN (right panel) as well as the NL AGN (left panel) in this work. As a comparison, we also put the result from the previous study by Lusso et al. (2012) in a grey symbol (BL AGN as filled square while NL AGN as open diamond). We add the upper limit value of black hole mass (the sources with irregular or no morphological type in the ZEST catalog) in an open square symbol in the left and right panel of Fig. 5.3. The upper limit values which are showed in open squares distributes in the same range as the remaining sources. The diagonal lines represent the relation between L_{bol} and M_{BH} at different Eddington ratios ($\lambda_{Edd} = 10^0, 10^{-1}, 10^{-2}$, and 10^{-3}). Typical errors of M_{BH} and L_{bol} are measured as 0.46 and 0.2, respectively.

As we can see in Fig. 5.3, our NL AGNs ($\log \lambda_{Edd} = -1.727 \pm 0.426$) show similar distribution as the NL AGNs from Lusso et al. (2012) ($\log \lambda_{Edd} = -1.72 \pm 0.59$) of which has slightly lower redshift sample ($z < 1.2$). The BL AGN sample is shown in a similar range of Eddington ratio but higher in black hole mass as well as the bolometric luminosity. Meanwhile, the OD AGNs show more scatter distribution than NL AGNs. The Eddington ratio of OD AGNs ($\log \lambda_{Edd} = -2.037 \pm 0.618$) are shwon slightly lower than NL AGN. However, we do not find

any difference between the diluted and undiluted populations among OD AGN distribution.

Trump et al. (2011a) mentioned that the accretion rates are supposed to be lower than of $\lambda_{\rm Edd} \lesssim 10^{-2}$ to avoid BLR forming due to RIAF disk in the inner radii of the accretion disk. As result, Trump et al. (2011b) and Pons et al. (2016) showed all of their OD AGNs had lower accretion rates than the limit of $\lambda_{\rm Edd} \lesssim 10^{-2}$. Instead, our result gives more scattered value in accretion rates compared to those studies. In our OD AGNs, 85 sources show accretion rates larger than the limiting Eddington ratio of 10^{-2} showing typical accretion rate of NL AGNs. Meanwhile, 95 OD AGNs still show lower accretion rates like typical RIAF disk sources.

In total, OD AGNs show systematically higher accretion rates than previous studies. We consider this difference come from the sample selection process. Trump et al. (2011b) had spectroscopic data with observational limit of $i_{\rm AB} \lesssim 23$ which might lack of fainter galaxies population compare to ours that give observational limit of $i_{\rm AB} \lesssim 25$. We also selected more distant galaxies in a deeper observation which is most likely to select lower mass galaxies. Furthermore, in contrast with our sample selection, their sample eliminated the emission-line galaxies, which is probably due to SF activity, from the OD AGN sample. As a result, our OD AGNs tend to have smaller $M_{\rm BH}$ galaxies and therefore show higher accretion rates. The difference with Pons et al. (2016) is most probably due to the X-ray luminosity limit to select the X-ray AGN being slightly lower than ours. They set the minimum values of $L_X \sim 10^{42}$ erg s^{-1} which is giving a lower bolometric luminosity then resulting in lower accretion rates.

Nevertheless, we could find a more significant number of OD AGNs that show a lower accretion rate of $\lambda_{\rm Edd} \lesssim 10^{-2}$ than previous studies. Even though the diluted sources may be a majority of these lower luminosity OD AGNs, we could still obtain large of OD AGs as good candidates of Radiatively Inefficient Accretion Flow (RIAF) sources.

Chapter 6

RIAF candidates

The last possibility of explaining the optical dullness is that these sources lack an optically thick accretion disk at small radii. Instead of a cool standard disk, at very low accretion rates, the gas at small radii of AGNs are expected to form a very hot radiatively inefficient accretion flow (RIAF, also known as an advection-dominated accretion flow, or ADAF). Unlike standard thin disks (Shakura and Sunyaev (1973)) in which the viscously generated energy is thermalized and radiated locally, RIAFs store most of the vicious energy and advect it into the SMBH. Due to the high temperatures and low densities, the particle in RIAFs is expected to generate broad-band, a multiwavelength electromagnetic spectrum from radio to γ-rays (e.g., Mahadevan et al. (1997), Manmoto et al. (1997), recent observation by de Menezes et al. (2020)). Alternatively, some authors have suggested that the BLR is in the inner part of the disk wind, and this wind is no longer supported at a low accretion rate. It will result in unobscured NL AGNs and OD AGNs, which were not showing the emission line due to the orientation effects but due to the lack of the BLR.Due to the absence of an optically thin disk at small radii, optical and UV emission of the RIAF sources would be very weak.

Table 6.1: OD AGNs most likely to host RIAF.

ID	Morphological type	$z_{\rm sp}$	$\log(M_{BH})$ ($M_\odot$)	$\log(L_{Bol})$ (erg s^{-1})	$\log(\lambda_{\rm Edd})$	VLA 3GHz detection
3014	elliptical	0.569	8.18	42.98	-3.3	x
3041	intermediate-bulge disc	0.36	7.99	43.46	-2.63	**V**
3298	intermediate-bulge disc	1.013	8.44	44.00	-2.54	**V**
3347	bulge-dominated disc	0.678	8.38	44.38	-2.09	**V**
3357	bulge-dominated disc	0.406	8.45	43.58	-2.96	x
3002	intermediate-bulge disc	0.853	8.08	42.9	-2.17	x
3062	disc-dominated	1.131	7.53	43.46	-2.17	**V**
3261	bulge-dominated disc	0.427	8.21	43.62	-2.69	**V**
3020	intermediate-bulge disc	0.425	8.06	43.26	-2.9	x

As we discussed in Chapter 5, we have 9 OD AGNs as RIAF candidates due to their low accretion rate and least possibly caused by host galaxy dilution or obscuration. The detailed parameters of these sources are written in Table 6.1). Moreover, these 9 OD AGNs have low hydrogen column densities of $N_{\rm H} < 10^{22}$ cm^{-2}, which is the typical value of unabsorbed BL AGNs. Tran (2003) discovered similar sources called "naked NL AGNs", which were characterized by a lack of a broad emission line even in a spectropolarimetry observation. The simple unified model cannot explain these sources from a viewing angle. They may have fundamentally different accretion physics like RIAF disk.

Low accretion rates OD AGNs can not be securely confirmed to host a RIAF based only on the accretion rate alone. We are required to discuss the sources most likely to have RIAF by comparing them with the RIAF model. RIAF model has characteristic emission in two primary wavelengths: radio and X-ray. The radio component is related to synchrotron emission, while the X-ray emission comes from the inverse Compton scattering.

This inner RIAF with an outer standard thin disk has been applied very well (and even required) to various black hole systems, including the supermassive black hole in our galactic Center, Sagittarius A* (Sgr A *) (Rees 1982, Narayan et al. 1995), low luminosity AGNs (LLAGNs) (Nemmen et al. (2014)), and Blackhole Binaries (BHBs) (Esin et al. (1997)) in the hard and quiescent states. Several studies have also predicted that an OD AGN lacks a standard accretion disc and instead is powered by a RIAF disk in the central region (e.g., Trump et al. (2011b)). It is supported by observational evidence through the lack of broad line emission even after being observed by spectropolarimetry. The study of OD AGN has also been done by Yuan and Narayan (2004) who successfully use the RIAF SED model as a fit model to their sources. They consider that many OD AGNs would possess RIAF disks.

RIAF is more common to be found in nearby LLAGNs. The occurrence of outflows in RIAFs can explain the weaker radiative outputs and large ratio of the X-ray to radio luminosities of LLAGNs (di Matteo et al. (2000)). Nemmen et al. (2014) presented nearby LLAGNs that have observed broadband spectrum are fitted into the RIAF model. Their sample had lower Eddington ratio than ours with typical value of $\lambda_{\rm Edd} \sim 10^{-5}$ due to their X-ray low luminosity ($L_X \sim 10^{40}$ erg s^{-1}). Similar to our OD AGNs, these LLAGNs do not have the optical signature of standard thin disk AGNs. Considering the similarity with these nearby LLAGNs, our OD AGNs seem to be the distant version of these sources, particularly the 9 RIAF candidate sources. The lower accretion rate of LLAGNs shows that there might be a possible growth of RIAF disk from our more distant OD AGNs into more local LLAGNs. It could support the natural decrease in quasar number counts at lower redshift since quasars may switch from a standard thin disk into a RIAF disk that is significantly less luminous and thus more difficult to detect.

An approach to confirm RIAF by broadband spectra SED fitting is likely to work on our sample. It is important to note that for fitting with the RIAF SED model, X-ray and radio

emission should be available on the targeting sources. The COSMOS project that also provides the available data by VLA observation (Smolčić et al. (2017)) is beneficial in this regard. Among these nine targets, five sources have been listed in the VLA COSMOS catalog (Smolčić et al. (2017)) (see Table 6.1 for finding the VLA detected sources). The possibility to find more OD AGNs that hosted the RIAF disk will give a complete picture of the evolution from a quasar in high redshift to the LLAGN in the very local universe.

Furthermore, RIAFs have been demonstrated to naturally accommodate hard X-ray emission, which gets along with gamma-ray emission. The gamma-ray emission in the innermost of our Galaxy (the confirmed RIAF source) is considered to be consistent with inverse Compton scattering by the RIAF disk. The Fermi Large Area Telescope also detects LLAGNs as a potential gamma-ray source (Abdo et al. (2009)). Using the RIAF model, we can predict the gamma-ray spectrum of our sources. It will be a good comparison with future Fermi detections.

Chapter 7

Summary

Using the multiwavelength catalog by the COSMOS project, we were able to study the NL AGN and OD AGN properties. We have presented optical diagnostic tools based on emission line and galaxy properties, allowing us to find the AGN signature in our sample up to redshift 1.5. We found 180 sources without AGN signatures in optical wavelengths, corresponding to a fraction of 60% of our X-ray-selected AGN sample.

One diagnostic tool for finding the AGN signature is finding the excess in the [O II] emission line. Unsurprisingly, we found a good relation of the [O II] luminosity ($L_{[\mathrm{O\ II}]}$) and the X-ray luminosity ($L_{2-10\mathrm{KeV}}$) among NL AGNs. Along with the previous study by Tanaka (2012) and Zakamska et al. (2003) data, the typical value X-ray to [O II] ratio ranges of $1 < R_{HX,[O\,\mathrm{II}]} < 2$. It shows us that the [O II] emission in these NL AGNs was coming from not only the SF region but also coming from the NLR of AGN. As one might expect, the relation cannot be addressed in our OD AGN sample, which confirmed that the [O II] emission is only coming from the SF region in the host galaxies.

The dilution scenario would easily explain the nature of optical dullness. By comparing the $R_{HX,[O\,\mathrm{II}]}$ value of our OD AGN sample and the typical NL AGN value, we could draw sources that are hosted by brighter galaxies. Besides that, the dilution can occur if we observe the entire galaxy placed in the spectroscopic aperture. The spectral observation of the entire galaxy and the bright host galaxy is the OD AGN's possible nature. Among our OD AGN case, the host galaxy dilution can explain $\sim 70\%$ of optical dullness. This fraction is similar with other authors proposal (Moran et al. (2002); Trump et al. (2009)).

Meanwhile, the high obscuration is least probably to explain the lack of optical AGN signatures in our case. The orientation, represented by the axial ratio, the OD AGN as well as NL AGN give no difference in distribution ranges from 0.2 to 1 (edge on to face on view). Besides that, based on hardness ratio value, the X-ray obscuration is less dense than typical Compton-thick clouds for all the samples. However, the obscured phase might be addressed to

the different nature of the OD AGN. Most of our undiluted sources are found to have absorbed X-rays. We can not rule out this fact.

The most interesting is whether optical dullness is due to the different intrinsic structures causing the low accretion rate. Hence, we estimated the Eddington ratio using black hole mass and bolometric luminosity estimation. The Eddington ratio is an essential parameter for detecting and identifying a galaxy as an AGN. We found that our estimators give an excellent result compared with previous work by Lusso et al. (2012), which have similar ranges and mean values of NL AGN in our work. Unlike Trump et al. (2011b) and Pons et al. (2016) that show all their OD AGNs give lower accretion rate than of $\log \lambda_{\rm Edd} \sim 2$, we still got half of our OD AGNs distribute in a higher Eddington ratio similar to typical BL AGN and NL AGN ($\log \lambda_{\rm Edd} \geq 2$) while the remaining half are below the limit. According to the sample selection, we come across more distant and fainter galaxies, most likely to result differently.

Finally, we found 9 sources that can not be explained by any dilution and do not seem to be obscured as an appropriate candidate of RIAF galaxies. We consider these OD AGNs most probably possess RIAF disks. It is helpful to place OD AGNs in the context of other accreting black hole sources, which better estimate the AGN population.

Acknowledgments

Acknowledgments

We would like to thank the referees of our doctoral thesis: Prof. Masayuki Akiyama, Prof. Hidekazu Tanaka, and Dr. Masaomi Tanaka for the fruitful discussion during the presentation of this work and all the detail comments as well as suggestions, which help us to improve this study. We also would like to thank Prof. Yoshiaki Taniguchi for his sincerity reviewing our draft and giving useful feedback. Itsna would also like to acknowledge the support from Japanese Goverment (Ministry of Education, Culture, Sports, Science, and Technology or MEXT) scholarship during which she study in Tohoku University.

This work is based on observation taken by COSMOS collaboration. More information on the COSMOS survey is available at http://www.astro.caltech.edu/ cosmos. It is a pleasure to acknowledge the available online archive for the COSMOS datasets. Some of the data present in this work also comes from previous study. We would like to thank Dr. Masayuki Tanaka and Dr. Elisabetta Lusso and are really appreciate their kindness for sharing their work data with us. This research also made use of Astropy (http://www.astropy.org), a community developed core Pyhton package for Astronomy and TOPCAT (http://www.starlink.ac.uk/topcat/).

Bibliography

Abdo, A. A., Ackermann, M., Ajello, M., Atwood, W. B., Axelsson, M., Baldini, L., Ballet, J., Barbiellini, G., Bastieri, D., Bechtol, K., and et al. (2009). Fermilarge area telescope gamma-ray detection of the radio galaxy m87. *The Astrophysical Journal*, 707(1):55–60.

Agostino, C. J. and Salim, S. (2019). Crossing the line: Active galactic nuclei in the star-forming region of the bpt diagram. *The Astrophysical Journal*, 876(1):12.

Antonucci, R. (1993). Unified models for active galactic nuclei and quasars. *Annual Review of Astronomy and Astrophysics*, 31(1):473–521.

Antonucci, R. and Miller, S. (1985). Spectropolarimetry and the nature of ngc 1068. *The Astrophysical Journal*, pages 621–632.

Astropy Collaboration, Price-Whelan, A. M., Sipőcz, B. M., Günther, H. M., Lim, P. L., Crawford, S. M., Conseil, S., Shupe, D. L., Craig, M. W., Dencheva, N., Ginsburg, A., Vand erPlas, J. T., Bradley, L. D., Pérez-Suárez, D., de Val-Borro, M., Aldcroft, T. L., Cruz, K. L., Robitaille, T. P., Tollerud, E. J., Ardelean, C., Babej, T., Bach, Y. P., Bachetti, M., Bakanov, A. V., Bamford, S. P., Barentsen, G., Barmby, P., Baumbach, A., Berry, K. L., Biscani, F., Boquien, M., Bostroem, K. A., Bouma, L. G., Brammer, G. B., Bray, E. M., Breytenbach, H., Buddelmeijer, H., Burke, D. J., Calderone, G., Cano Rodríguez, J. L., Cara, M., Cardoso, J. V. M., Cheedella, S., Copin, Y., Corrales, L., Crichton, D., D'Avella, D., Deil, C., Depagne, É., Dietrich, J. P., Donath, A., Droettboom, M., Earl, N., Erben, T., Fabbro, S., Ferreira, L. A., Finethy, T., Fox, R. T., Garrison, L. H., Gibbons, S. L. J., Goldstein, D. A., Gommers, R., Greco, J. P., Greenfield, P., Groener, A. M., Grollier, F., Hagen, A., Hirst, P., Homeier, D., Horton, A. J., Hosseinzadeh, G., Hu, L., Hunkeler, J. S., Ivezić, Ž., Jain, A., Jenness, T., Kanarek, G., Kendrew, S., Kern, N. S., Kerzendorf, W. E., Khvalko, A., King, J., Kirkby, D., Kulkarni, A. M., Kumar, A., Lee, A., Lenz, D., Littlefair, S. P., Ma, Z., Macleod, D. M., Mastropietro, M., McCully, C., Montagnac, S., Morris, B. M., Mueller, M., Mumford, S. J., Muna, D., Murphy, N. A., Nelson, S., Nguyen, G. H., Ninan, J. P., Nöthe, M., Ogaz, S., Oh, S., Parejko, J. K., Parley, N., Pascual, S., Patil, R., Patil, A. A., Plunkett, A. L., Prochaska, J. X.,

Rastogi, T., Reddy Janga, V., Sabater, J., Sakurikar, P., Seifert, M., Sherbert, L. E., Sherwood-Taylor, H., Shih, A. Y., Sick, J., Silbiger, M. T., Singanamalla, S., Singer, L. P., Sladen, P. H., Sooley, K. A., Sornarajah, S., Streicher, O., Teuben, P., Thomas, S. W., Tremblay, G. R., Turner, J. E. H., Terrón, V., van Kerkwijk, M. H., de la Vega, A., Watkins, L. L., Weaver, B. A., Whitmore, J. B., Woillez, J., Zabalza, V., and Astropy Contributors (2018). The Astropy Project: Building an Open-science Project and Status of the v2.0 Core Package. , 156(3):123.

Baldwin, J. A., Phillips, M. M., and Terlevich, R. (1981). Classification parameters for the emission-line spectra of extragalactic objects. *The Astrophysical Journal*, 93(551):5–19.

Brightman, M. and Nandra, K. (2008). On the nature of unabsorbed seyfert 2 galaxies. *Monthly Notices of the Royal Astronomical Society*, 390(3):1241–1249.

Brusa, M., Comastri, A., Mignoli, M., Fiore, F., Ciliegi, P., Vignali, C., Severgnini, P., Cocchia, F., La Franca, F., Matt, G., and et al. (2003). The hellas2xmm survey. *Astronomy Astrophysics*, 409(1):65–78.

Caccianiga, A., Severgnini, P., Della Ceca, R., Maccacaro, T., Carrera, F. J., and Page, M. J. (2007). Elusive agn in thexmm-newtonbright serendipitous survey. *Astronomy Astrophysics*, 470(2):557–570.

Civano, F., Mignoli, M., Comastri, A., Vignali, C., Fiore, F., Pozzetti, L., Brusa, M., La Franca, F., Matt, G., Puccetti, S., and et al. (2007). The hellas2xmm survey. *Astronomy Astrophysics*, 476(3):1223–1233.

Comastri, A., Mignoli, M., Ciliegi, P., Severgnini, P., Maiolino, R., Brusa, M., Fiore, F., Baldi, A., Molendi, S., Morganti, R., and et al. (2002). The hellas2xmmsurvey. ii. multiwavelength observations of p3: An x-ray–bright, optically inactive galaxy. *The Astrophysical Journal*, 571(2):771–778.

de Menezes, R., Nemmen, R., Finke, J. D., Almeida, I., and Rani, B. (2020). Gamma-ray observations of low-luminosity active galactic nuclei. *Monthly Notices of the Royal Astronomical Society*, 492(3):4120–4130.

di Matteo, T., Quataert, E., Allen, S. W., Narayan, R., and Fabian, A. C. (2000). Low-radiative-efficiency accretion in the nuclei of elliptical galaxies. *Monthly Notices of the Royal Astronomical Society*, 311(3):507–521.

Esin, A. A., McClintock, J. E., and Narayan, R. (1997). Advection-dominated accretion and the spectral states of black hole x-ray binaries: Application to nova muscae 1991. *The Astrophysical Journal*, 489(2):865–889.

Graham, A. W. (2007). The black hole mass - spheroid luminosity relation. *Monthly Notices of the Royal Astronomical Society*, 379(2):711–722.

Hasinger, G., Capak, P., Salvato, M., Barger, A. J., Cowie, L. L., Faisst, A., Hemmati, S., Kakazu, Y., Kartaltepe, J., Masters, D., and et al. (2018). The deimos 10k spectroscopic survey catalog of the cosmos field. *The Astrophysical Journal*, 858(2):77.

Hawkins, M. R. S. (2004). Naked active galactic nuclei. *Astronomy Astrophysics*, 424(2):519–529.

Heckman, T. M. and Best, P. N. (2014). The coevolution of galaxies and supermassive black holes: Insights from surveys of the contemporary universe. *Annual Review of Astronomy and Astrophysics*, 52(1):589–660.

Juneau, S., Bournaud, F., Charlot, S., Daddi, E., Elbaz, D., Trump, J. R., Brinchmann, J., Dickinson, M., Duc, P.-A., Gobat, R., and et al. (2014). Active galactic nuclei emission line diagnostics and the mass-metallicity relation up to redshiftz 2: The impact of selection effects and evolution. *The Astrophysical Journal*, 788(1):88.

Juneau, S., Dickinson, M., Alexander, D. M., and Salim, S. (2011). A NEW DIAGNOSTIC OF ACTIVE GALACTIC NUCLEI: REVEALING HIGHLY ABSORBED SYSTEMS AT REDSHIFT 0.3. *The Astrophysical Journal*, 736(2):104.

Kennicutt, R. C. (1998). Star formation in galaxies along the hubble sequence. *Annual Review of Astronomy and Astrophysics*, 36(1):189–231.

Kormendy, J. and Richstone, D. (1995). Inward bound—the search for supermassive black holes in galactic nuclei. *Annual Review of Astronomy and Astrophysics*, 33(1):581–624.

Laigle, C., McCracken, H. J., Ilbert, O., Hsieh, B. C., Davidzon, I., Capak, P., Hasinger, G., Silverman, J. D., Pichon, C., Coupon, J., Aussel, H., Le Borgne, D., Caputi, K., Cassata, P., Chang, Y.-Y., Civano, F., Dunlop, J., Fynbo, J., Kartaltepe, J. S., Koekemoer, A., Le Fèvre, O., Le Floc'h, E., Leauthaud, A., Lilly, S., Lin, L., Marchesi, S., Milvang-Jensen, B., Salvato, M., Sanders, D. B., Scoville, N., Smolcic, V., Stockmann, M., Taniguchi, Y., Tasca, L., Toft, S., Vaccari, M., and Zabl, J. (2016). The cosmos2015 catalog: Exploring the 1 lt; z lt; 6 universe with half a million galaxies. *The Astrophysical Journal Supplement Series*, 224(2):24.

Lilly, S. J., Fevre, O. L., Renzini, A., Zamorani, G., Scodeggio, M., Contini, T., Carollo, C. M., Hasinger, G., Kneib, J., Iovino, A., and et al. (2007). zcosmos: A large vlt/vimos redshift survey covering 0 ¡ z ¡ 3 in the cosmos field. *The Astrophysical Journal Supplement Series*, 172(1):70–85.

Lusso, E., Comastri, A., Simmons, B. D., Mignoli, M., Zamorani, G., Vignali, C., Brusa, M., Shankar, F., Lutz, D., Trump, J. R., and et al. (2012). Bolometric luminosities and eddington ratios of x-ray selected active galactic nuclei in thexmm-cosmos survey. *Monthly Notices of the Royal Astronomical Society*, 425(1):623–640.

Läsker, R., Ferrarese, L., van de Ven, G., and Shankar, F. (2013). Supermassive black holes and their host galaxies. ii. the correlation with near-infrared luminosity revisited. *The Astrophysical Journal*, 780(1):70.

Maccacaro, T., Gioia, I. M., Wolter, A., Zamorani, G., and Stocke, J. T. (1998). THE X-RAY SPECTRA OF THE EXTRAGALACTIC SOURCES IN THE EINSTEIN EXTENDED MEDIUM SENSITIVITY SURVEY. *The Astrophysical Journal*, 326(1):680–690.

Mahadevan, R., Narayan, R., and Krolik, J. (1997). Gamma-ray emission from advection-dominated accretion flows around black holes: Application to the galactic center. *The Astrophysical Journal*, 486(1):268–275.

Maiolino, R., Comastri, A., Gilli, R., Nagar, N. M., Bianchi, S., Boker, T., Colbert, E., Krabbe, A., Marconi, A., Matt, G., and et al. (2003). Elusive active galactic nuclei. *Monthly Notices of the Royal Astronomical Society*, 344(4):L59–L64.

Maiolino, R., Marconi, A., Salvati, M., Risaliti, G., Severgnini, P., Oliva, E., La Franca, F., and Vanzi, L. (2001). Dust in active nuclei. *Astronomy Astrophysics*, 365(2):28–36.

Manmoto, T., Mineshige, S., and Kusunose, M. (1997). Spectrum of optically thin advection-dominated accretion flow around a black hole: Application to sagittarius a*. *The Astrophysical Journal*, 489(2):791–803.

Marchesi, S., Civano, F., Elvis, M., Salvato, M., Brusa, M., Comastri, A., Gilli, R., Hasinger, G., Lanzuisi, G., Miyaji, T., Treister, E., Urry, C. M., Vignali, C., Zamorani, G., Allevato, V., Cappelluti, N., Cardamone, C., Finoguenov, A., Griffiths, R. E., Karim, A., Laigle, C., LaMassa, S. M., Jahnke, K., Ranalli, P., Schawinski, K., Schinnerer, E., Silverman, J. D., Smolcic, V., Suh, H., and Trakhtenbrot, B. (2016). THECHANDRA COSMOS LEGACYSURVEY: OPTICAL/IR IDENTIFICATIONS. *The Astrophysical Journal*, 817(1):34.

Marconi, A. and Hunt, L. K. (2003). The relation between black hole mass, bulge mass, and near-infrared luminosity. *The Astrophysical Journal*, 589(1):L21–L24.

Marconi, A., Risaliti, G., Gilli, R., Hunt, L. K., Maiolino, R., and Salvati, M. (2004). Local supermassive black holes, relics of active galactic nuclei and the X-ray background. *Monthly Notices of the Royal Astronomical Society*, 351(1):169–185.

McCracken, H. J., Milvang-Jensen, B., Dunlop, J., Franx, M., Fynbo, J. P. U., Le Fèvre, O., Holt, J., Caputi, K. I., Goranova, Y., Buitrago, F., and et al. (2012). Ultravista: a new ultra-deep near-infrared survey in cosmos. *Astronomy Astrophysics*, 544:A156.

Merloni, A., Bongiorno, A., Brusa, M., Iwasawa, K., Mainieri, V., Magnelli, B., Salvato, M., Berta, S., Cappelluti, N., Comastri, A., and et al. (2013). The incidence of obscuration in active galactic nuclei. *Monthly Notices of the Royal Astronomical Society*, 437(4):3550–3567.

Mignoli, M., Vignali, C., Gilli, R., Comastri, A., Zamorani, G., Bolzonella, M., Bongiorno, A., Lamareille, F., Nair, P., Pozzetti, L., and et al. (2013). Obscured agn atz 1 from the zcosmos-bright survey. *Astronomy Astrophysics*, 556:A29.

Mineo, S., Gilfanov, M., and Sunyaev, R. (2011). X-ray emission from star-forming galaxies - i. high-mass x-ray binaries. *Monthly Notices of the Royal Astronomical Society*, 419(3):2095–2115.

Moran, E. C., Filippenko, A. V., and Chornock, R. (2002). "hidden" seyfert 2 galaxies and the x-ray background. *The Astrophysical Journal*, 579(2):L71–L74.

Narayan, R., Mahadevan, R., and Quartert, E. (1998). Advection-dominated accretion around black holes. pages 148–182.

Narayan, R., Sadowski, A., Penna, R. F., and Kulkarni, A. K. (2012). Grmhd simulations of magnetized advection-dominated accretion on a non-spinning black hole: role of outflows. *Monthly Notices of the Royal Astronomical Society*, 426(4):3241–3259.

Nemmen, R. S., Storchi-Bergmann, T., and Eracleous, M. (2014). Spectral models for low-luminosity active galactic nuclei in liners: the role of advection-dominated accretion and jets. *Monthly Notices of the Royal Astronomical Society*, 438(4):2804–2827.

Nemmen, R. S., Storchi-Bergmann, T., Yuan, F., Eracleous, M., Terashima, Y., and Wilson, A. S. (2006). Radiatively inefficient accretion flow in the nucleus of ngc 1097. *The Astrophysical Journal*, 643(2):652–659.

Netzer, H., Mainieri, V., Rosati, P., and Trakhtenbrot, B. (2006). The correlation of narrow line emission and x-ray luminosity in active galactic nuclei. *Astronomy Astrophysics*, 453(2):525–533.

Padovani, P., Alexander, D. M., Assef, R. J., De Marco, B., Giommi, P., Hickox, R. C., Richards, G. T., Smolčić, V., Hatziminaoglou, E., Mainieri, V., and et al. (2017). Active galactic nuclei: what's in a name? *The Astronomy and Astrophysics Review*, 25(1).

Pons, E., Elvis, M., Civano, F., and Watson, M. G. (2016). NARROW-LINE x-RAY-SELECTED GALAXIES IN THECHANDRA-COSMOS FIELD. II. OPTICALLY ELUSIVE x-RAY AGNs. *The Astrophysical Journal*, 824(1):51.

Pouliasis, E., Mountrichas, G., Georgantopoulos, I., Ruiz, A., Yang, M., and Bonanos, A. Z. (2020). An obscured agn population hidden in the vipers galaxies: identification through spectral energy distribution decomposition. *Monthly Notices of the Royal Astronomical Society*, 495(2):1853–1873.

Rigby, J. R., Rieke, G. H., Donley, J. L., Alonso-Herrero, A., and Perez-Gonzalez, P. G. (2006). Why x-ray-selected active galactic nuclei appear optically dull. *The Astrophysical Journal*, 645(1):115–133.

Sanders, D. B., Salvato, M., Aussel, H., Ilbert, O., Scoville, N., Surace, J. A., Frayer, D. T., Sheth, K., Helou, G., Brooke, T., and et al. (2007). S-cosmos: The spitzer legacy survey of the hubble space telescope acs 2 deg 2 cosmos field i: Survey strategy and first analysis. *The Astrophysical Journal Supplement Series*, 172(1):86–98.

Scarlata, C., Carollo, C. M., Lilly, S., Sargent, M. T., Feldmann, R., Kampczyk, P., Porciani, C., Koekemoer, A., Scoville, N., Kneib, J.-P., Leauthaud, A., Massey, R., Rhodes, J., Tasca, L., Capak, P., Maier, C., McCracken, H. J., Mobasher, B., Renzini, A., Taniguchi, Y., Thompson, D., Sheth, K., Ajiki, M., Aussel, H., Murayama, T., Sanders, D. B., Sasaki, S., Shioya, Y., and Takahashi, M. (2007). COSMOS morphological classification with the zurich estimator of structural types (ZEST) and the evolution since z = 1 of the luminosity function of early, disk, and irregular galaxies. *The Astrophysical Journal Supplement Series*, 172(1):406–433.

Scoville, N., Aussel, H., Brusa, M., Capak, P., Carollo, C. M., Elvis, M., Giavalisco, M., Guzzo, L., Hasinger, G., Impey, C., and et al. (2007). The cosmic evolution survey (cosmos): Overview. *The Astrophysical Journal Supplement Series*, 172(1):1–8.

Severgnini, P., Caccianiga, A., Braito, V., Della Ceca, R., Maccacaro, T., Wolter, A., Sekiguchi, K., Sasaki, T., Yoshida, M., Akiyama, M., and et al. (2003). Xmm-newtonobservations reveal agn in apparently normal galaxies. *Astronomy Astrophysics*, 406(2):483–492.

Shakura, N. I. and Sunyaev, R. A. (1973). Black holes in biunary systems. observational appearance. *Astron. Astrophys*, 24:337–335.

Smolčić, V., Delvecchio, I., Zamorani, G., Baran, N., Novak, M., Delhaize, J., Schinnerer, E., Berta, S., Bondi, M., Ciliegi, P., and et al. (2017). The vla-cosmos 3 ghz large project: Multiwavelength counterparts and the composition of the faint radio population. *Astronomy Astrophysics*, 602:A2.

Tanaka, M. (2012). A method of identifying agns based on emission-line excess and the nature of low-luminosity agns in the sloan digital sky survey. i. a new method. *Publications of the Astronomical Society of Japan*, 64(2):36.

Taniguchi, Y., Kajisawa, M., Kobayashi, M. A. R., Shioya, Y., Nagao, T., Capak, P. L., Aussel, H., Ichikawa, A., Murayama, T., Scoville, N. Z., and et al. (2015). The subaru cosmos 20: Subaru optical imaging of the hst cosmos field with 20 filters. *Publications of the Astronomical Society of Japan*, 67(6):104.

Taniguchi, Y., Scoville, N., Murayama, T., Sanders, D. B., Mobasher, B., Aussel, H., Capak, P., Ajiki, M., Miyazaki, S., Komiyama, Y., and et al. (2007). The cosmic evolution survey (cosmos): Subaru observations of the hst cosmos field. *The Astrophysical Journal Supplement Series*, 172(1):9–28.

Tran, H. D. (2003). The unified model and evolution of active galaxies: Implications from a spectropolarimetric study. *The Astrophysical Journal*, 583(2):632–648.

Trouille, L., Barger, A. J., and Tremonti, C. (2011). THE OPTX PROJECT. v. IDENTIFYING DISTANT ACTIVE GALACTIC NUCLEI. *The Astrophysical Journal*, 742(1):46.

Trump, J. R., Impey, C. D., Kelly, B. C., Civano, F., Gabor, J. M., Diamond-Stanic, A. M., Merloni, A., Urry, C. M., Hao, H., Jahnke, K., and et al. (2011a). Accretion rate and the physical nature of unobscured active galaxies. *The Astrophysical Journal*, 733(1):60.

Trump, J. R., Impey, C. D., Taniguchi, Y., Brusa, M., Civano, F., Elvis, M., Gabor, J. M., Jahnke, K., Kelly, B. C., Koekemoer, A. M., Nagao, T., Salvato, M., Shioya, Y., Capak, P., Huchra, J. P., Kartaltepe, J. S., Lanzuisi, G., McCarthy, P. J., Maineri, V., and Scoville, N. Z. (2009). THE NATURE OF OPTICALLY DULL ACTIVE GALACTIC NUCLEI IN COSMOS. *The Astrophysical Journal*, 706(1):797–809.

Trump, J. R., Nagao, T., Ikeda, H., Murayama, T., Impey, C. D., Stocke, J. T., Civano, F., Elvis, M., Jahnke, K., Kelly, B. C., and et al. (2011b). Spectropolarimetric evidence for radiatively inefficient accretion in an optically dull active galaxy. *The Astrophysical Journal*, 732(1):23.

Vika, M., Driver, S. P., Cameron, E., Kelvin, L., and Robotham, A. (2011). The near-ir mbh-l and mbh-n relations. *Monthly Notices of the Royal Astronomical Society*, 419(3):2264–2292.

Yi, I. (1996). Cosmological evolution of quasars. *The Astrophysical Journal*, 473(2):645–650.

Yuan, F. and Narayan, R. (2004). On the nature of x-ray–bright, optically normal galaxies. *The Astrophysical Journal*, 612(2):724–728.

Zakamska, N. L., Strauss, M. A., Heckman, T. M., Ivezić, , and Krolik, J. H. (2004). Candidate type ii quasars from the sloan digital sky survey. ii. from radio to x-rays. *The Astronomical Journal*, 128(3):1002–1016.

Zakamska, N. L., Strauss, M. A., Krolik, J. H., Collinge, M. J., Hall, P. B., Hao, L., Heckman, T. M., Ivezi, e., Richards, G. T., Schlegel, D. J., and et al. (2003). Candidate type ii quasars from the sloan digital sky survey. i. selection and optical properties of a sample at 0.3¡z¡0.83. *The Astronomical Journal*, 126(5):2125–2144.

Zamojski, M. A., Schiminovich, D., Rich, R. M., Mobasher, B., Koekemoer, A. M., Capak, P., Taniguchi, Y., Sasaki, S. S., McCracken, H. J., Mellier, Y., and et al. (2007). Deep galex imaging of the cosmos hst field: A first look at the morphology of z 0.7 star-forming galaxies. *The Astrophysical Journal Supplement Series*, 172(1):468–493.

Appendix A

Appendix

A.1 AGN data

The properties reported in these tables are listed below.

1. *Column 1.* Object ID sequence number based on this study.
2. *Column 2 - 3.* Position (J2000) of the objects in unit degree.
3. *Column 4.* Spectroscopic redshift (Marchesi et al. 2016).
4. *Column 5.* i-band AB magnitude.
5. *Column 6.* The X-ray and optical flux comparison which are explained in equation 2.2.
6. *Column 7.* Logarithmic scale of rest-frame luminosity in full band (0.5–10 keV) (erg s^{-1})
7. *Column 8.*Logarithmic scale of [OII] luminosity obtained by measuring the optical spectra line (erg s^{-1})
8. *Column 9.* Hardness Ratio, (H-S)/(H+S)(Marchesi et al. 2016).
9. *Column 10-11.* Stellar mass (M_*) in the unit of M$\odot$ and star formation rate (SFR) in the unit of M$\odot$ yr^{-1} from BC03 best-fit template in logarithmic scale. Taken at the minimum χ^2 (Laigle et al. 2016).
10. *Column 12.* Axis ratio (b/a = (semi-minor axis / semi major axis)).
11. *Column 13.* Radii of the galaxy defined as the semi-major axis length of ellipse encompassing 50% of total light ($''$).
12. *Column 14.* Bolometric luminosity in logarithmic scale ((erg s^{-1}))

13. *Column 15.* Blackhole mass in logarithmic scale (M$\odot$).

14. *Column 16.* Eddington ratio ($\lambda_{\rm Edd} = \frac{L_{\rm bol}}{L_{\rm Edd}}$).

15. *Column 17.* Spectral type of AGN. BL–Broad line, NL– Narrow Line, OD–Optically Dull

Table A.1: AGN sample data in this work

ID	RA (deg)	DEC (deg)	z_{sp}	i_{AB} (mag)	X/O	$L_{0.5-10keV}$ (erg s^{-1})	L[OII] (erg s^{-1})	HR	log(M_*) ($M_\odot$)	log(SFR) ($M_\odot$yr^{-1})	b/a	$r_{1/2}$ ($''$)	L_{bol} (erg s^{-1})	log(M_{BH}) ($M_\odot$)	λ_{Edd}	type
3002	150.507	2.654	0.8093	21.17	-1.74	42.55		-99.00	11.03	1.79	0.89	0.66	42.90	8.69	-3.89	OD
3003	150.250	2.215	0.497	20.41	-1.60	42.88	40.09	0.55	11.09	0.18	0.59	0.67	44.10	8.60	-2.59	OD
3004	149.867	1.748	0.562	20.86	-1.55	42.73	42.32	-0.01	10.62	2.24	0.34	0.95				OD
3005	150.241	2.348	0.7031	21.74	-1.54	42.67	41.86	-0.14	10.87	1.20	0.42	0.29				OD
3010	149.862	2.173	0.8844	21.63	-1.44	42.86	42.47	0.10	11.26	1.59	0.88	0.32	43.95	9.00	-3.15	OD
3011	149.638	1.907	0.691	21.04	-1.42	42.62	41.99	0.34	10.90	1.43	0.73	0.33	43.58	8.65	-3.16	OD
3014	149.997	2.416	0.5696	20.86	-1.40	42.48		-0.54	10.82	0.56	0.82	0.51	42.98	8.59	-3.71	OD
3015	149.687	2.183	0.6328	20.83	-1.39	42.62	42.10	0.04	10.73	1.92	0.46	0.91	43.57	8.56	-3.09	OD
3016	149.692	1.818	0.7378	20.75	-1.38	43.01		0.23	11.38	-0.17	0.40	0.62	44.10	8.74	-2.73	OD
3017	150.001	1.541	0.893	22.19	-1.38	42.98	42.03	0.36	10.90	1.06						OD
3018	150.501	1.829	0.8814	21.71	-1.37	42.55	41.80	-99.00	11.15	0.60	0.60	0.33	43.09	8.64	-3.65	OD
3019	150.478	1.790	0.7022	20.91	-1.37	43.03		0.37	10.64	-2.09	0.84	0.26	44.17	8.37	-2.29	OD
3020	150.514	2.040	0.425	19.98	-1.34	42.51	42.55	-0.43	11.00	1.13	0.61	1.28	43.26	8.46	-3.30	OD
3025	149.572	2.263	0.706	20.91	-1.32	43.34	42.95	0.71	11.10	0.37	0.68	0.34	44.62	8.68	-2.15	NL
3031	149.890	1.920	1.329	22.17	-1.23	43.20	43.18	0.03	10.66	1.90	0.75	0.25				OD
3033	150.348	2.080	0.9302	21.94	-1.22	42.78		-0.10	11.00	-0.56	0.89	0.23	43.20	8.74	-3.64	OD
3034	150.113	2.009	1.182	22.91	-1.22	42.88	41.66	0.07	11.08	1.23	0.70	0.21	44.07	8.60	-2.62	OD
3035	149.868	2.219	0.7894	21.84	-1.19	42.64	41.77	-0.27	11.16	-0.39	0.61	0.31	43.11	8.57	-3.56	NL
3036	149.793	2.781	0.7037	21.89	-1.18	43.33		0.67	10.79	0.10	0.48	0.34	44.62	8.28	-1.75	OD
3037	150.122	2.526	0.606	21.19	-1.17	42.67		-99.00	11.12	-0.43	0.59	0.38	43.64	8.55	-3.01	OD
3040	149.644	2.561	1.0004	21.62	-1.16	43.33	42.61	0.43	10.93	2.01	0.86	0.23	44.46	8.73	-2.36	OD
3041	150.234	1.945	0.3605	19.79	-1.15	42.71	43.32	-0.41	10.93	0.99	0.76	0.54	43.46	8.42	-3.06	OD
3042	150.507	2.575	0.6264	22.02	-1.15	42.86		0.56	10.83	0.35	0.26	0.68	44.08	8.34	-2.35	OD
3044	149.945	2.494	1.0256	21.47	-1.14	43.10	43.11	-0.29	10.51	1.91	0.81	0.70	43.49	8.70	-3.33	OD
3045	149.966	2.033	0.728	21.94	-1.14	42.54	42.24	-99.00	11.38	0.65	0.41	0.41	43.05	8.66	-3.70	NL
3048	150.396	2.058	0.9647	21.56	-1.13	43.03	42.16	-99.00	11.42	2.10	0.64	0.43	44.00	8.97	-3.07	OD
3049	150.245	2.356	1.1033	22.23	-1.13	42.94		-99.00	11.20	1.70	0.47	0.49	43.34	8.77	-3.52	OD
3050	150.003	2.134	0.958	22.07	-1.13	42.93	42.37	-0.09	11.22	0.67	0.81	0.22	43.96	8.79	-2.92	OD
3051	149.681	2.268	0.902	22.59	-1.12	42.84	41.80	-99.00	10.75	-0.37	0.77	0.28	44.02	8.18	-2.25	NL
3052	150.019	2.148	0.9588	21.39	-1.12	43.58	42.53	0.56	11.07	1.57	0.63	0.46				NL
3053	150.599	2.781	0.431	21.09	-1.12	42.58	40.84	0.02	10.62	-0.67	0.87	0.29	43.56	8.17	-2.70	OD
3055	150.075	1.660	0.7475	21.85	-1.11	42.86	41.50	0.36	10.67	1.00	0.74	0.31	43.86	8.34	-2.57	OD
3056	149.721	2.665	0.741	21.97	-1.10	42.61		-0.19	10.95	-0.17	0.36	0.48	43.42	8.33	-3.01	OD
3057	149.909	2.706	0.886	22.28	-1.10	42.65	41.99	-0.39	10.76	-1.23	0.48	0.22	43.14	8.31	-3.27	NL
3058	149.883	2.172	1.002	21.8	-1.09	42.90	41.69	-0.57	11.23	-0.77	0.84	0.31	43.46	8.66	-3.30	NL
3061	149.912	1.923	0.775	21.76	-1.08	43.01	42.06	0.18	11.06	0.15	0.56	0.42	44.13	8.57	-2.54	NL
3062	150.581	2.023	1.131	22.16	-1.06	42.85	42.36	-99.00	10.75	2.00	0.50	0.66	43.46	8.40	-3.03	OD
3063	149.738	1.979	0.526	21.67	-1.06	43.27	40.97	0.77	10.66	0.40	0.30	0.75	44.56	8.24	-1.78	OD
3065	149.490	2.656	0.4707	20.76	-1.05	42.70		-0.21	10.81	-0.09	0.54	0.46	43.50	8.39	-2.99	OD

Table A.2: AGN sample data in this work

ID	RA (deg)	DEC (deg)	z_{sp}	i_{AB} (mag)	X/O	$L_{0.5-10keV}$ (erg s^{-1})	L[OII] (erg s^{-1})	HR	log(M_*) ($M_\odot$)	log(SFR) ($M_\odot$yr^{-1})	b/a	$r_{1/2}$ ($''$)	L_{bol} (erg s^{-1})	log(M_{BH}) ($M_\odot$)	λ_{Edd}	type
3067	149.788	1.929	1.2463	22.77	-1.04	42.83		-0.18	10.93	1.44	0.83	0.30	43.32	8.73	-3.51	OD
3068	150.155	1.690	0.9139	21.47	-1.04	42.95		-0.49	11.18	-0.39	0.90	0.30	43.69	8.88	-3.29	OD
3070	150.040	2.471	0.6786	21.97	-1.04	43.13	41.39	0.57	10.56	0.01	0.74	0.23	44.40	8.20	-1.90	OD
3073	149.911	2.098	0.8851	22.41	-1.03	42.66	41.98	-0.60	10.47	1.34	0.63	0.31	43.15	8.33	-3.27	OD
3074	149.891	1.944	0.6675	21.46	-1.03	42.92	41.49	-0.02	10.91	0.00	0.53	0.47	43.92	8.46	-2.63	OD
3075	150.023	2.207	0.9402	21.96	-1.03	42.97	41.84	-99.00	10.88	1.52	0.95	0.42	43.40	8.56	-3.26	OD
3076	149.724	2.268	1.029	22.29	-1.03	43.02	42.12	0.11	10.83	1.44	0.63	0.36	44.08	8.55	-2.56	OD
3077	150.077	2.428	0.7507	22.09	-1.02	42.77	41.72	-0.24	10.98	0.24	0.58	0.32	43.14	8.37	-3.33	OD
3078	149.730	2.071	0.8833	22.4	-1.01	42.77		-0.10	10.82	-1.18	0.76	0.23	43.18	8.58	-3.50	OD
3079	149.612	2.354	1.376	24.03	1.01	44.43		-0.28	11.20	0.94	0.73	0.10				NL
3081	149.583	2.046	0.819	22.5		42.51	41.94	-99.00	10.73	0.88	0.36	0.41	43.76	8.34	-2.68	NL
3082	150.239	1.984	0.5112	20.92		42.51	41.65	-99.00	10.45	-0.68	0.79	0.36	43.80	8.36	-2.66	NL
3083	149.857	2.273	0.764	21.12		42.51	41.98	0.67	11.09	1.42	0.77	0.54	43.73	8.65	-3.01	OD
3084	150.477	2.494	0.6793	21.13		42.54	42.37	-99.00	10.54	-0.04	0.83	0.35	43.72	8.47	-2.85	NL
3087	150.459	2.733	0.793	21.55		42.59		-99.00	11.39	0.27	0.56	0.60	43.83	8.66	-2.92	OD
3088	149.928	2.535	0.669	20.76		42.60	41.55	-99.00	10.77	-0.36	0.64	0.42	43.86	8.37	-2.60	NL
3090	150.511	1.963	0.88	22.01		42.60	42.47	0.18	10.69	1.02	0.76	0.31	43.65	8.58	-3.02	OD
3093	150.443	2.230	0.865	23.01		42.65	39.50	-99.00	10.81	0.96	0.30	0.46	43.78	8.40	-2.72	OD
3095	150.122	2.000	1.059	23.52		42.66		0.22	11.14	0.67	0.45	0.19	43.94	8.57	-2.72	OD
3096	149.666	2.222	0.8934	21.89		42.66	43.16	0.36	11.24	1.39	0.76	0.32		8.95		NL
3098	150.395	2.639	0.9259	22.3		42.68	42.10	0.29	11.14	0.94	0.62	0.30	43.94	8.56	-2.73	OD
3099	149.831	1.902	0.7302	21.59		42.69	42.18	-99.00	10.96	0.27	0.73	0.22	43.81	8.40	-2.69	NL
3102	149.793	2.423	1.025	21.95		42.71	42.19	-99.00	10.86	1.65	0.75	0.39		8.61		NL
3103	150.223	2.501	0.991	23.12		42.71	41.95	0.55	10.90	-0.22	0.32	0.36	43.93	8.30	-2.47	NL
3105	149.850	2.452	0.7138	21.58		42.72	41.49	0.40	10.81	0.12	0.80	0.24	43.92	8.51	-2.69	OD
3107	150.582	2.440	0.881	22.87		42.75	41.63	0.36	10.50	-1.06	0.61	0.18	43.89	8.14	-2.35	NL
3109	150.526	2.422	1.061	23.01		42.75	42.47	0.47	10.19	2.47	0.44	0.46	43.85	8.23	-2.48	OD
3110	149.937	2.300	0.934	22.65		42.76	41.97	-99.00	10.72	1.36	0.52	0.47	44.09	8.22	-2.22	NL
3111	149.975	2.140	0.9574	22.39		42.77	42.37	-99.00	10.68	2.11	0.55	0.81		8.36		OD
3113	149.937	1.739	0.864	22.06		42.78	42.15	-99.00	10.91	0.36	0.58	0.27	44.07	8.46	-2.49	NL
3114	150.095	2.889	0.815	22.43		42.79	41.61	-99.00	10.66	1.16						NL
3117	150.077	2.043	1.18	23.93		42.82	41.48	-99.00	10.59	-1.40	0.62	0.15	44.11	8.18	-2.17	OD
3118	150.382	2.753	1.148	23.7		42.82	42.27	-0.10	10.26	1.46	0.62	0.43				OD
3120	149.645	1.968	0.8795	22.71		42.85	41.68	-99.00	10.55	0.68	0.59	0.31		8.23		OD
3121	150.312	1.730	0.5785	20.65		42.86	42.32	-99.00	10.78	1.54	0.50	0.89	44.17	8.52	-2.45	OD
3122	150.111	2.330	1.253	24.23		42.86	42.27	-99.00	10.51	-1.06	0.68	0.14		8.15		NL
3123	149.697	1.905	0.6606	20.77		42.87	42.22	-99.00	10.67	1.61	0.72	0.55	44.12	8.63	-2.60	NL
3125	150.520	2.424	0.881	22		42.88	42.44	-99.00	10.92	-0.64	0.57	0.31	44.12	8.59	-2.57	NL
3126	149.564	2.030	0.724	21.73		42.88	41.66	-99.00	10.81	1.76	0.36	0.23				OD
3127	150.137	2.274	1.2175	22.35		42.89	42.47	-99.00	11.32	0.19	0.63	0.24	44.17	9.01	-2.94	NL
3128	149.960	1.608	1.274	23.65		42.89	42.73	-0.47	10.46	1.41						OD

Table A.3: AGN sample data in this work

ID	RA (deg)	DEC (deg)	z_{sp}	i_{AB} (mag)	X/O	$L_{0.5-10keV}$ (erg s^{-1})	L[OII] (erg s^{-1})	HR	log(M_*) ($M_\odot$)	log(SFR) ($M_\odot$yr^{-1})	b/a	$r_{1/2}$ ($''$)	L_{bol} (erg s^{-1})	log(M_{BH}) ($M_\odot$)	λ_{Edd}	type
3130	149.921	2.250	0.881	21.54		42.94	42.11	-99.00	10.93	1.57	0.85	0.29	44.18	8.60	-2.51	NL
3131	150.581	2.092	1.238	24.07		42.94	42.63	0.00	10.97	0.49	0.68	0.13	44.01	8.44	-2.53	NL
3132	150.317	1.658	0.684	21.26		42.95	42.36	0.55	10.84	0.36	0.64	0.36	44.18	8.47	-2.39	NL
3133	150.083	1.659	1.413	24.25		42.95		-99.00	10.97	0.71	0.81	0.13				OD
3134	150.508	2.667	1.488	24.32		42.96		-99.00	10.98	1.25	0.94	0.07				OD
3135	149.771	2.729	1.236	23.57		42.99	42.74	-99.00	10.27	1.50	0.89	0.11	44.19	8.26	-2.17	OD
3137	150.546	1.822	1.209	23.98		43.07	42.24	-99.00	10.63	1.71	0.57	0.22	44.37	8.23	-1.96	OD
3138	149.926	1.596	0.772	22.05		43.07		0.82	10.50	1.55						NL
3139	150.077	2.511	1.244	23.68		43.09	42.82	0.41	10.27	1.73	0.97	0.10		8.28		NL
3144	150.009	2.026	1.193	23.05		43.19	42.67	0.41	10.99	2.01	0.48	0.49	44.44	8.75	-2.40	NL
3145	150.419	1.719	0.998	22.35		43.20	42.28	0.77	11.12	0.65	0.62	0.40	44.43	8.56	-2.22	NL
3146	150.157	2.089	1.129	24.4		43.22	42.26	0.78	10.69	0.84	0.58	0.21				OD
3147	150.392	1.677	1.235	23.76		43.22	42.50	0.42	10.82	1.69	0.79	0.15	44.37	8.59	-2.32	NL
3149	150.231	1.571	0.828	21.42		43.24	42.57	-99.00	11.32	0.77						NL
3150	150.253	1.871	1.376	24.28		43.28	42.53	0.44	10.69	-0.87	0.59	0.17				NL
3151	149.496	2.066	1.449	23.99		43.30	42.95	-99.00	10.54	1.22	0.45	0.18		8.31		NL
3152	150.109	2.132	1.253	24.03		43.35	42.26	0.73	11.00	0.10	0.92	0.19				NL
3153	150.679	2.310	1.082	23.64		43.39	41.94	0.32	10.97	0.07	0.71	0.15	44.47	8.38	-2.00	OD
3154	149.931	1.735	1.427	24.22		43.53	43.29	0.77	10.59	0.01	0.83	0.13				NL
3156	149.974	1.644	1.0301	21.3	-0.99	43.27		-0.18	11.00	2.41	0.79	0.38	44.20	9.09	-2.99	OD
3159	150.266	2.759	1.258	22.72	-0.97	43.62	42.99	0.71	10.98	1.77	0.85	0.26	44.94	8.64	-1.80	OD
3160	149.734	2.691	0.9105	21.02	-0.97	43.24	43.80	-0.50	10.11	2.48	0.55	0.39				OD
3161	150.667	2.347	0.982	22.12	-0.95	43.05	42.23	-0.37	11.18	0.28	0.88	0.19	43.90	8.76	-2.96	NL
3171	149.442	2.288	0.476	20.64	-0.89	43.16	41.55	0.30	11.22	-0.33						BL
3174	150.591	2.176	1.263	22.49	-0.83	43.49	42.71	0.52	10.90	1.76	0.80	0.11				OD
3176	150.547	2.811	0.746	22.6	-0.81	42.41		-99.00	10.62	-0.72	0.73	0.16				OD
3177	149.810	2.576	0.972	22.87	-0.81	43.15	42.47	0.57	10.23	-0.10	0.69	0.17	44.37	8.28	-2.01	NL
3178	149.712	2.365	1.0293	22.01	-0.79	43.39	42.63	0.28	10.99	1.86	0.80	0.24	44.58	8.83	-2.35	OD
3182	149.730	2.255	1.0122	22.48	-0.72	43.27		0.31	11.01	1.16	0.50	0.31	44.42	8.68	-2.36	OD
3184	150.098	2.008	1.0922	22.61	-0.68	43.10		-0.53	10.68	1.93	0.83	0.27	43.86	8.57	-2.81	OD
3186	150.436	2.161	1.3	23.41	-0.67	43.37	42.57	0.67	10.71	1.86	0.47	0.26	44.58	8.58	-2.10	OD
3190	150.180	2.110	0.3597	19.18	-0.65	43.45		-0.40	10.38	2.15	0.49	0.98				BL
3193	149.731	2.368	0.834	22.93	-0.64	42.74	41.94	-0.39	10.76	-0.15	0.87	0.16	43.27	8.44	-3.27	NL
3194	150.405	2.278	1.354	23.42	-0.63	-43.58	42.45	-99.00	10.74	1.90	0.84	0.15	43.56	8.61	-3.14	OD
3195	149.744	2.250	0.1333	17.93	-0.63	43.00	41.64	-0.24	10.72	0.49	0.86	1.17	43.89	8.38	-2.59	BL
3196	149.702	2.730	1.2761	22.68	-0.62	43.27	42.87	-0.23	11.20	1.81	0.80	0.35				OD
3202	150.140	1.817	0	21.94	-0.52	44.09	42.62	-0.35	10.77	2.40	0.68	0.35	45.11	8.73	-1.71	NL
3203	149.808	1.709	0.9551	21.99	-0.51	43.39		-0.49	10.10	2.29	0.94	0.12				OD
3208	149.945	2.078	0.8886	22.77	-0.45	43.10		-0.41	10.76	0.20	0.62	0.21	43.88	8.23	-2.45	OD
3212	150.187	1.992	1.245	23.63	-0.39	42.98	41.97	-0.61	10.06	2.19	0.86	0.14	43.65	8.32	-2.77	OD

Table A.4: AGN sample data in this work

ID	RA (deg)	DEC (deg)	z_{sp}	i_{AB} (mag)	X/O	$L_{0.5-10keV}$ (erg s^{-1})	L[OII] (erg s^{-1})	HR	log(M_*) ($M_\odot$)	log(SFR) ($M_\odot$yr^{-1})	b/a	$r_{1/2}$ ($''$)	L_{bol} (erg s^{-1})	log(M_{BH}) ($M_\odot$)	λ_{Edd}	type
3214	149.675	1.912	1.3145	22.49	-0.36	43.97		0.38	11.16	1.77	0.45	0.52	45.28	8.80	-1.62	OD
3217	150.050	1.744	1.1485	21.76	-0.35	43.76	42.70	-99.00	10.68	2.14	0.89	0.19	44.42	8.87	-2.55	OD
3219	150.259	1.757	0.9652	21.53	-0.33	43.83		-0.23	10.72	2.13	0.58	0.27				OD
3222	149.461	2.346	1.1231	22.08	-0.24	43.92		0.03	11.47	1.80						NL
3226	150.446	2.044	1.1713	21.41	-0.09	44.27		-0.21	10.41	2.79	0.83	0.12				BL
3228	150.353	1.932	1.373	23.25	-0.07	43.75	42.28	-0.13	10.98	1.62	0.89	0.14				OD
3229	149.730	2.454	1.1005	22.16	-0.06	43.96		-0.27	10.45	1.83	0.91	0.10				OD
3234	150.318	2.602	0.9576	21	-0.01	44.30	41.94	-0.26	10.23	2.50	0.95	0.14				NL
3235	149.660	2.411	1.1608	21.8	0.01	44.18	42.38	-0.14	10.84	2.30	0.88	0.18				NL
3236	150.555	2.641	1.1442	21.55	0.04	44.26		-0.24	10.32	2.70	0.56	0.16				BL
3238	150.422	2.175	0.979	20.88	0.07	44.43	42.34	-0.42	10.00	2.66	0.65	0.14				BL
3239	149.895	2.174	1.3226	22.22	0.07	44.19		-0.37	10.32	2.98	0.97	0.08				BL
3240	150.041	2.563	1.442	24.84	0.14	43.44	42.49	-99.00	10.97	0.71	0.67	0.18				NL
3242	149.979	2.309	1.456	24.42	0.16	43.79	43.04	0.20	10.88	1.67	0.54	0.35	45.00	8.34	-1.45	OD
3247	149.701	2.403	0.3758	20.95	0.30	43.82		-0.08	10.61	-0.68	0.58	0.24	44.82	8.03	-1.30	BL
3248	150.082	2.058	0.893	23.58	0.30	43.53	40.37	-0.34	10.04	-0.86	0.40	1.57	44.38	7.68	-1.40	OD
3250	150.415	1.934	1.175	25.01	0.39	44.34	41.70	-0.13	10.48	0.98	0.59	0.27				OD
3252	150.353	2.133	1.297	24.12	0.52	44.06	43.19	0.13	10.53	1.17	0.86	0.11	45.30	8.52	-1.32	NL
3253	149.850	2.398	1.189	23.57	0.56	44.08	42.46	-0.34	10.11	2.30	0.88	0.08				NL
3257	150.212	2.402	0.905	22.16	-1.00	42.91	41.98	-0.13	11.21	0.30	0.80	0.19	43.93	8.78	-2.95	OD
3259	150.228	2.270	0.6776	21.17	-0.99	43.01	42.40	-0.14	10.77	1.64	0.45	0.82				OD
3260	149.702	2.122	0.89	22.04	-0.98	42.95	42.30	0.13	11.13	0.01	0.60	0.34	44.09	8.47	-2.48	NL
3261	149.864	1.776	0.4266	20.31	-0.98	42.81		-0.17	10.92	-0.18	0.44	0.79	43.62	8.41	-2.89	OD
3262	149.737	2.264	1.242	22.74	-0.98	43.00	43.01	-99.00	10.38	2.07	0.77	0.40				OD
3263	150.406	2.518	0.876	21.7	-0.97	43.26	42.25	0.14	10.76	1.91	0.52	0.67				NL
3264	150.370	2.042	0.9755	21.89	-0.97	42.99	42.08	-99.00	10.92	1.62	0.58	0.25	43.52	8.77	-3.34	OD
3265	149.975	2.315	0.8525	21.95	-0.97	42.92	42.34	-0.20	10.42	1.79	0.56	0.58				OD
3268	149.762	2.180	0.3396	20.39	-0.95	42.67		-0.24	10.77	-0.90	0.75	0.39	43.53	8.24	-2.81	OD
3270	150.120	2.117	0.958	21.91	-0.93	43.06		-0.23	11.13	-0.43	0.74	0.34	44.00	8.62	-2.71	OD
3272	150.400	2.688	0.2158	19.11	-0.93	42.69	41.53	-0.26	10.41	1.27	0.89	1.31				BL
3274	150.324	2.004	0.9555	21.63	-0.93	43.13	41.84	-0.34	10.81	2.15	0.79	0.34	43.62	8.80	-3.28	OD
3275	150.714	2.314	0.6077	20.77	-0.93	43.11	41.91	-0.08	11.34	-0.21	0.37	0.58	44.01	8.71	-2.80	NL
3276	149.787	2.378	0.7659	22.26	-0.92	42.71		-0.39	10.78	-0.34	0.86	0.23	43.68	8.43	-2.85	OD
3277	150.113	2.175	0.9866	22.26	-0.92	42.85	42.53	-0.48	10.32	1.73	0.85	0.38	43.43	8.14	-2.81	OD
3279	149.663	2.270	0.6755	20.69	-0.92	43.25		-0.02	11.46	-0.30	0.67	0.37	44.19	8.78	-2.69	OD
3280	150.493	2.116	0.845	21.92	-0.92	42.88	41.99	-0.23	11.03	0.34	0.69	0.41	43.43	8.59	-3.26	OD
3281	149.673	2.629	0.5942	21.29	-0.91	42.79	41.53	-0.35	10.80	0.24	0.50	0.49	43.54	8.37	-2.93	OD
3282	150.005	2.633	0.6775	20.78	-0.91	43.21		-0.14	11.09	0.54	0.97	0.33	44.14	8.69	-2.65	OD
3283	149.813	1.824	0.5303	21.13	-0.90	42.78	41.85	-0.32	10.64	0.60	0.86	0.21	43.61	8.39	-2.88	OD
3284	149.884	2.338	1.0222	21.9	-0.90	43.72	43.19	0.62	10.61	1.99	0.78	0.35				NL
3285	150.106	2.213	0.9248	22.5	-0.89	42.83	41.65	-0.34	10.65	1.30	0.40	0.43	43.30	8.39	-3.18	OD

Table A.5: AGN sample data in this work

ID	RA (deg)	DEC (deg)	z_{sp}	i_{AB} (mag)	X/O	$L_{0.5-10keV}$ (erg s^{-1})	L[OII] (erg s^{-1})	HR	log(M_*) (M$_\odot$)	log(SFR) (M$_\odot$yr^{-1})	b/a	$r_{1/2}$ ($''$)	L_{bol} (erg s^{-1})	log(M_{BH}) (M$_\odot$)	λ_{Edd}	type
3286	150.373	2.203	1.172	22.79	-0.89	42.93	42.21	-0.38	10.98	-0.15	0.39	0.33				NL
3287	149.573	2.711	0.867	22.22	-0.88	43.20	41.97	0.48	11.14	0.02	0.84	0.14	44.35	8.48	-2.22	NL
3289	150.288	2.404	0.6565	21.55	-0.87	43.00	41.90	0.01	10.58	-1.42	0.62	0.27	44.04	8.31	-2.36	NL
3290	149.650	2.209	0.953	21.87	-0.86	43.03	42.53	-0.04	11.28	-0.71	0.77	0.42	43.97	8.84	-2.96	NL
3291	149.643	2.726	0.3935	20.33	-0.86	43.16		0.43	10.91	-0.38	0.27	0.59	44.25	8.25	-2.09	OD
3292	149.953	2.660	0.892	21.77	-0.86	43.12	42.10	-0.05	11.10	-0.90	0.88	0.30	44.03	8.79	-2.85	NL
3293	150.006	1.897	0.793	22.41	-0.85	42.84	41.45	-0.10	10.81	-0.10	0.78	0.17	43.85	8.25	-2.50	NL
3294	150.391	2.087	0.9612	22.35	-0.85	42.98	42.10	-0.40	11.13	0.65	0.60	0.24				OD
3295	149.858	1.746	0.6672	21.1	-0.85	43.09		-0.30	11.20	0.08	0.77	0.36	43.93	8.75	-2.91	OD
3296	150.491	2.635	0.3458	19.82	-0.84	43.02		0.09	10.78	0.31	0.86	0.66	43.98	8.30	-2.42	OD
3297	150.318	2.234	0.3737	20.98	-0.84	42.60		-0.37	10.25	-0.22	0.75	0.32	43.38	8.04	-2.75	OD
3298	150.209	2.575	0.9971	21.79	-0.84	43.19	42.35	-0.39	11.34	1.48	0.69	0.57	44.00	8.82	-2.92	OD
3300	150.472	2.849	1.202	22.41	-0.82	43.12	41.11	-0.61	11.07	0.22	0.92	0.17	43.67	8.61	-3.04	NL
3301	149.494	2.040	0.979	22.84	-0.81	43.17	42.45	0.48	10.73	1.48	0.60	0.19	44.30	8.60	-2.40	NL
3302	150.588	1.948	1.249	23.17	-0.80	42.99		0.03	10.99	2.07	0.69	0.27	43.41	8.72	-3.41	OD
3303	150.150	2.475	0.689	20.82	-0.80	43.72	42.41	0.52	10.76	1.92	0.73	0.47	45.04	8.62	-1.68	NL
3304	150.387	1.952	1.373	23.16	-0.80	42.86	42.84	-99.00	10.98	1.39	0.71	0.31	43.51	8.61	-3.20	OD
3306	149.813	2.802	0.8845	21.83	-0.79	43.35	41.52	0.39	11.02	0.29	0.79	0.24	44.46	8.62	-2.25	NL
3307	150.009	2.627	1.001	22.19	-0.78	43.18	42.23	-0.20	11.06	1.21	0.79	0.37	44.14	8.58	-2.54	NL
3310	150.062	2.659	0.437	20.23	-0.77	43.03	41.53	-0.41	11.23	0.32	0.96	1.08	43.83	8.79	-3.06	NL
3311	149.618	2.216	0.6761	21.29	-0.77	43.08	41.68	-0.39	10.57	1.56	0.61	0.63	43.88	8.40	-2.62	OD
3312	150.002	2.461	0.732	22.1	-0.77	42.82	41.91	-0.35	10.54	-1.45	0.70	0.16	43.37	8.37	-3.10	NL
3314	150.753	2.345	0.9668	21.72	-0.76	43.63	42.80	0.50	11.07	0.22						NL
3317	150.305	2.053	1.178	22.52	-0.76	43.45	42.18	0.21	11.09	1.79	0.51	0.44				NL
3318	150.015	2.666	1.176	22.63	-0.75	43.84	42.57	0.71	11.30	0.83	0.70	0.33	45.23	8.69	-1.56	NL
3319	149.950	1.683	0.7764	22.71	-0.75	42.99	41.73	0.44	10.57	1.60	0.59	0.31	44.10	8.40	-2.40	OD
3320	149.779	2.233	0.7621	21.52	-0.75	43.24		-0.03	10.92	-2.37	0.55	0.28	44.29	8.52	-2.32	OD
3321	150.115	2.582	0.8926	22.04	-0.75	43.17	42.05	-0.07	10.67	0.82	0.91	0.16	44.13	8.29	-2.26	OD
3323	149.658	2.323	1.008	22.75	-0.74	42.95	42.71	-0.28	10.67	1.05	0.88	0.16	43.85	8.52	-2.76	NL
3325	150.668	1.616	0.3725	20.52	-0.73	43.05		0.20	10.71	-0.20	0.59	0.60	44.06	8.27	-2.31	OD
3326	149.837	1.972	1.02	23.36	-0.73	42.92	42.69	-0.02	10.77	2.05	0.39	0.42	43.99	8.61	-2.72	OD
3327	150.118	1.586	0.84	22.42	-0.72	43.28	42.26	0.51	10.77	-1.79	0.83	0.26	44.49	8.43	-2.03	NL
3329	150.538	2.789	1.1993	22.91	-0.72	43.11	42.86	-0.19	10.22	2.04	0.65	0.35	43.56	8.36	-2.89	OD
3331	150.601	2.519	0.668	21.96	-0.71	43.05	41.13	0.08	10.34	0.48	0.94	0.18	44.04	8.30	-2.36	OD
3332	150.129	1.921	1.0095	22.39	-0.71	43.26		0.02	10.68	1.33	0.93	0.17	44.35	8.54	-2.30	OD
3336	149.961	2.218	0.7344	20.98	-0.70	43.47	42.20	-0.08	10.80	1.82	0.64	0.57	44.49	8.58	-2.18	OD
3337	150.366	2.400	0.9878	22.05	-0.70	43.27	41.72	-0.26	10.74	0.16	0.28	0.32				OD
3339	149.668	2.135	0.3393	19.84	-0.69	43.03	42.35	-0.44	10.58	1.10	0.66	0.99	43.77	8.41	-2.74	NL
3340	150.484	2.829	0.95	22.36	-0.69	43.21	41.67	0.07	10.90	1.98	0.62	0.38	44.35	8.66	-2.40	NL
3342	150.092	2.719	0.9038	22.77	-0.68	42.92	42.64	0.03	10.03	1.31	0.40	0.55	43.98	7.89	-2.01	OD
3343	150.138	2.292	0.184	19.12	-0.68	42.81		-0.40	10.74	0.27	0.29	2.25	43.58	8.27	-2.79	BL

Table A.6: AGN sample data in this work

ID	RA (deg)	DEC (deg)	z_{sp}	i_{AB} (mag)	X/O	$L_{0.5-10keV}$ (erg s^{-1})	L[OII] (erg s^{-1})	HR	log(M_*) ($M_\odot$)	log(SFR) ($M_\odot$yr^{-1})	b/a	$r_{1/2}$ ($''$)	L_{bol} (erg s^{-1})	log(M_{BH}) ($M_\odot$)	λ_{Edd}	type
3344	150.112	2.125	0.959	23.56	-0.67	42.57	42.37	-99.00	10.49	1.00	0.67	0.23	43.13	8.24	-3.21	OD
3345	150.492	1.773	0.8326	21.16	-0.67	43.71	42.33	0.28	10.66	2.44	0.74	0.21				NL
3346	150.596	2.365	1.082	22.62	-0.67	43.03	41.91	0.03	10.80	-0.34	0.82	0.19	43.64	8.62	-3.08	OD
3347	149.738	2.065	0.6776	20.61	-0.67	43.49	41.61	-0.29	11.11	1.94	0.55	0.59	44.38	8.90	-2.61	OD
3350	149.978	2.504	1.171	23.16	-0.65	43.13	42.06	0.13	10.83	-0.30	0.89	0.14	44.37	8.64	-2.37	NL
3352	150.232	1.628	0.404	20.46	-0.64	43.04	43.14	-0.42	10.63	0.76	0.51	0.65	43.86	8.29	-2.53	OD
3353	150.564	1.901	1.395	23.45	-0.64	43.13	42.66	-0.01	10.82	2.97	0.51	0.13				NL
3354	149.957	2.479	1.028	22.89	-0.64	42.92	42.00	-99.00	10.34	1.49	0.95	0.21	43.51	8.30	-2.88	OD
3355	150.589	2.097	1.16	23.41	-0.63	42.94	42.48	-0.23	10.24	1.83	0.66	0.17	43.86	8.45	-2.68	NL
3357	150.473	2.198	0.404	20.35	-0.62	43.02	40.95	-0.60	11.24	0.51	0.71	0.61	43.58	8.70	-3.21	OD
3358	150.047	2.108	0.4798	20.73	-0.62	43.16		-0.37	10.49	1.44	0.54	0.49	43.93	8.36	-2.53	NL
3359	149.691	2.336	0.8643	21.96	-0.62	43.39	41.74	0.12	11.02	-0.10	0.81	0.24	44.50	8.38	-1.98	NL
3360	150.056	2.233	0.9376	21.33	-0.61	43.63		-0.17	11.27	1.60	0.44	0.69	44.59	8.79	-2.30	OD
3361	150.223	1.807	0.5304	21.71	-0.61	42.95		-0.15	10.28	0.03	0.71	0.29	43.88	8.10	-2.31	OD
3362	150.300	1.784	0.7069	21.41	-0.61	43.24		-0.44	10.98	0.08	0.81	0.28	44.04	8.61	-2.66	OD
3363	149.920	2.514	0.698	21.92	-0.60	43.06	41.80	-0.41	10.29	-0.85	0.65	0.15	43.82	8.01	-2.29	NL
3365	150.067	2.643	0.6933	22.19	-0.57	42.99		-0.57	10.60	-0.74	0.56	0.21	43.67	8.05	-2.47	OD
3367	150.412	2.474	1.2645	23.01	-0.56	43.47	41.99	0.30	11.14	-0.42	0.74	0.16	44.64	8.63	-2.09	NL
3368	150.022	2.517	0.6787	21.29	-0.56	43.50	42.12	0.11	11.23	0.11	0.34	0.74	44.60	8.68	-2.17	OD
3370	149.859	2.108	1.245	23.2	-0.56	43.60	42.21	0.46	11.13	0.66	0.43	0.41				OD
3374	149.477	2.582	0.4191	21.26	-0.54	42.83		-0.42	10.35	0.41	0.62	0.23	43.75	8.09	-2.44	OD
3375	150.295	2.275	1.353	23.29	-0.52	43.13	42.67	-99.00	10.56	1.71	0.47	0.35				OD
3376	149.695	2.653	0.317	21.01	-0.52	42.69	42.04	-0.27	10.06	1.01	0.24	1.23	43.50	7.79	-2.38	NL
3377	150.334	2.457	0.876	23.04	-0.52	43.03	41.80	-0.20	10.49	-0.06	0.93	0.13	43.92	8.24	-2.41	NL
3378	149.559	1.631	0.9009	21.84	-0.51	43.31		-0.60	11.26	0.78	0.90	0.19				OD
3384	149.521	2.079	0.6752	21.19	-0.49	43.39	42.28	-0.36	10.99	1.13	0.61	0.28	44.26	8.59	-2.42	NL
3386	150.591	2.128	0.724	23.47	-0.48	42.57	41.09	0.05	10.18	-0.73	0.89	0.10				NL
3387	149.642	2.476	1.1733	22.01	-0.48	43.84	42.80	0.21	10.72	2.26	0.88	0.41	45.02	8.79	-1.86	NL
3388	150.435	2.143	0.967	21.91	-0.48	43.56	42.27	-0.14	10.92	1.78	0.81	0.29	44.57	8.86	-2.39	NL
3389	150.245	2.844	1.258	22.61	-0.47	43.36	42.96	-99.00	10.84	2.03	0.72	0.24	44.02	8.81	-2.89	OD
3391	149.579	2.002	0.987	22.45	-0.47	43.31		-0.31	11.04	-0.08	0.67	0.18	43.84	8.53	-2.79	OD
3392	150.171	2.337	1.26	24.03	-0.47	43.35	42.61	0.38	10.68	0.65	0.68	0.14				NL
3394	150.199	2.598	0.901	21.94	-0.46	43.59	42.44	0.15	11.10	-1.47	0.49	0.32	44.69	8.54	-1.95	NL
3395	150.482	2.834	1.26	23.47	-0.46	43.25	42.73	-0.53	10.45	1.79	0.85	0.34	43.65	8.22	-2.67	OD
3396	149.586	1.769	0.7855	22.06	-0.45	43.74	42.30	0.61	10.71	2.52	0.88	0.20				NL
3397	150.616	2.079	1.424	23.56	-0.45	43.17	42.99	-0.54	10.75	1.36	0.29	0.29	43.75	8.49	-2.84	OD
3398	149.993	1.858	0.834	21.81	-0.45	43.36	42.08	-0.62	11.12	0.65	0.82	0.36	43.93	8.78	-2.94	OD
3399	149.940	2.140	1.478	23.83	-0.44	43.49	42.37	0.31	10.80	-0.33	0.82	0.10				NL
3400	150.044	1.757	0.735	22.83	-0.44	42.90	42.33	-0.17	10.41	-0.93	0.83	0.15	43.75	7.90	-2.25	NL
3401	149.884	2.212	1.155	23.09	-0.44	43.28	41.79	-0.22	10.67	1.00	0.72	0.30	44.24	8.33	-2.19	NL
3403	150.511	2.029	0.8991	21.21	-0.43	43.82	43.58	-0.05	10.80	2.39	0.73	0.28				NL
3405	150.631	2.255	1.43	24.18	-0.43	43.53	42.73	0.51	10.64	-0.21	0.68	0.13	44.81	8.52	-1.80	NL

Table A.7: AGN sample data in this work

ID	RA (deg)	DEC (deg)	z_{sp}	i_{AB} (mag)	X/O	$L_{0.5-10keV}$ (erg s^{-1})	L[OII] (erg s^{-1})	HR	log(M_*) (M$_\odot$)	log(SFR) (M$_\odot$yr^{-1})	b/a	$r_{1/2}$ ($''$)	L_{bol} (erg s^{-1})	log(M_{BH}) (M$_\odot$)	λ_{Edd}	type
3408	150.080	2.266	1.405	23.6	-0.41	43.45	42.01	0.23	11.07	0.81	0.67	0.17	44.73	8.33	-1.70	OD
3410	149.721	2.360	1.193	24.16	-0.41	43.45	41.53	0.59	10.64	1.50	0.80	0.41				NL
3411	150.235	2.216	1.368	23.76	-0.40	43.41	41.73	0.22	11.12	1.45	0.45	0.26	44.66	8.67	-2.11	OD
3412	150.593	2.539	1.138	22.67	-0.40	43.29	42.92	-0.46	11.17	1.13	0.86	0.19	43.97	8.89	-3.02	NL
3413	150.129	1.923	1.005	22.66	-0.39	43.34	42.28	-0.28	10.92	1.24	0.56	0.32	44.23	8.65	-2.51	OD
3414	149.862	1.895	0.4445	19.73	-0.39	43.80		0.05	11.12	0.86	0.67	0.91	44.70	8.82	-2.22	NL
3415	149.959	2.356	0.889	22.3	-0.39	43.37	41.86	-0.28	10.18	1.99	0.88	0.17				OD
3417	149.548	2.078	0.961	23.43	-0.39	42.97		-0.02	10.38	0.01	0.85	0.14	43.48	7.96	-2.58	OD
3418	149.827	2.397	0.9106	22.64	-0.39	43.46	41.76	0.18	10.85	1.00	0.44	0.30	44.62	8.43	-1.91	NL
3420	149.564	1.963	1.118	24.01	-0.37	42.96	43.39	-0.50	10.48	1.65	0.49	0.21	43.93	8.40	-2.57	OD
3421	150.280	1.744	0.7627	22.38	-0.36	43.14		-0.63	10.62	0.07	0.69	0.20	43.76	8.11	-2.44	OD
3422	150.052	2.306	1.463	23.35	-0.36	43.64	42.51	0.12	11.08	2.02	0.86	0.10	44.80	9.00	-2.30	NL
3423	150.646	2.350	1.09	23.28	-0.36	43.53	43.63	0.52	10.99	2.09	0.75	0.18	44.67	8.51	-1.93	OD
3424	149.850	2.132	1.48	23.58	-0.34	43.26	42.48	-99.00	10.72	2.21	0.90	0.18	43.90	8.64	-2.83	OD
3427	150.086	1.674	1.116	23.25	-0.29	43.38		0.30	10.79	0.94	0.81	0.17	44.34	8.61	-2.37	OD
3429	150.150	2.864	1.329	23.47	-0.28	43.28	42.82	-99.00	10.59	2.22	0.48	0.15	43.90	8.82	-3.01	OD
3431	150.607	1.935	0.68	21.99	-0.27	43.30	42.74	-0.19	11.15	-0.40	0.67	0.39	44.13	8.57	-2.53	OD
3432	150.443	2.323	1.371	23.27	-0.25	43.65	43.15	0.01	10.93	1.09	0.47	0.34	44.77	8.49	-1.82	NL
3433	150.418	2.085	0.4246	20.49	-0.25	43.48		-0.27	10.11	2.38	0.90	0.34	44.33	8.62	-2.39	BL
3434	149.855	2.132	0.956	22.37	-0.24	43.47	41.80	-0.56	10.36	1.82	0.70	0.19				NL
3435	149.599	2.589	0.947	24.1	-0.24	42.97	41.75	0.21	10.12	-1.45	0.78	0.13	44.02	7.86	-1.93	NL
3436	149.822	2.152	1.052	23.26	-0.23	43.30	41.87	-0.45	10.88	-2.41	0.54	0.23	44.04	8.36	-2.41	NL
3438	150.587	2.199	1.425	23.82	-0.22	43.32	43.75	-0.46	10.26	2.16	0.52	0.30	44.25	8.20	-2.04	NL
3439	149.683	2.384	0.959	24	-0.22	43.00	41.62	-0.21	10.38	1.13	0.30	0.32	43.41	8.21	-2.90	OD
3440	149.868	2.455	1.313	24.12	-0.22	43.08	42.16	-99.00	10.63	1.24	0.81	0.10	43.86	8.62	-2.86	OD
3441	149.597	2.441	1.1684	22.79	-0.22	43.78	43.23	0.46	10.26	2.45	0.73	0.30	44.82	8.49	-1.77	NL
3442	149.559	2.181	1.176	23.75	-0.21	43.43	42.01	0.44	10.80	0.95	0.77	0.15	44.50	8.39	-1.99	OD
3443	150.379	1.959	1.047	23.98	-0.21	43.12		-0.13	10.65	1.52	0.34	0.28	44.10	8.24	-2.23	OD
3444	149.768	2.431	0.9444	21.37	-0.19	44.09	42.64	-0.14	11.36	0.81	0.56	0.40	45.27	8.80	-1.63	NL
3445	149.571	1.684	0.5487	21.79	-0.17	43.24	42.16	-0.37	10.31	-0.06	0.76	0.17	43.96	7.91	-2.04	NL
3447	150.488	2.150	0.876	23.1	-0.17	43.23	42.21	-99.00	10.31	1.40	0.71	0.21	44.06	8.27	-2.30	NL
3448	150.095	2.634	1.182	23.43	-0.16	43.42	41.08	-0.17	10.44	0.11	0.93	0.11				OD
3449	150.538	2.311	0.8391	21.71	-0.14	43.88	42.38	0.03	10.64	1.58	0.43	0.64	45.00	8.45	-1.56	OD
3450	150.281	1.955	1.238	23.86	-0.14	43.26		-0.42	10.75	2.20	0.31	0.22	44.11	8.42	-2.41	OD
3451	150.048	2.374	0.937	23.6	-0.14	43.07	41.82	-0.58	10.57	0.10	0.73	0.18	43.74	8.15	-2.50	NL
3454	150.265	2.008	0.85	22.74	-0.11	43.41	42.19	-0.34	10.07	1.37	0.69	0.14				NL
3455	150.536	2.684	1.213	23.5	-0.10	43.58	42.14	0.11	10.86	1.00	0.79	0.16				OD
3456	149.815	1.635	1.475	24.01	-0.10	43.52	43.65	-0.17	10.62	2.20	0.90	0.08				OD
3458	150.434	2.225	1.1795	24.16	-0.06	43.21	42.36	-0.48	10.45	-1.11	0.80	0.12	43.70	8.11	-2.51	NL
3460	150.672	1.760	1.1749	22.56	-0.03	44.00	43.32	-0.02	10.97	0.12	0.81	0.19	44.96	8.67	-1.81	NL
3461	149.849	2.384	1.314	24.2	-0.03	43.31	42.63	-0.38	10.83	0.35	0.81	0.15	44.21	8.34	-2.22	NL

Table A.8: AGN sample data in this work

ID	RA (deg)	DEC (deg)	z_{sp}	i_{AB} (mag)	X/O	$L_{0.5-10keV}$ (erg s^{-1})	L[OII] (erg s^{-1})	HR	log(M_*) (M$_\odot$)	log(SFR) (M$_\odot$yr^{-1})	b/a	$r_{1/2}$ ($''$)	L_{bol} (erg s^{-1})	log(M_{BH}) (M$_\odot$)	λ_{Edd}	type
3462	150.559	2.177	0.868	22.77	-0.02	43.45	41.55	-0.23	10.27	1.37	0.47	0.28	44.29	8.23	-2.03	OD
3463	150.203	2.380	1.258	24.8	-0.02	43.20	41.64	-0.12	10.67	0.19	0.48	0.21				NL
3464	150.374	2.460	1.28	21.97	-0.02	44.22	42.70	-0.20	11.43	1.89	0.34	1.43				NL
3465	149.693	2.267	0.905	22.76	-0.01	43.54	41.85	-0.17	10.75	0.20	0.75	0.17	44.12	8.34	-2.32	NL
3467	150.431	1.988	0.976	23.44	0.00	43.67	41.97	0.42	10.49	1.51	0.26	0.54	44.92	8.12	-1.30	OD
3469	150.655	1.996	0.979	22.35	0.01	43.73	41.39	-0.37	10.83	1.62	0.92	0.23	44.52	8.77	-2.35	OD
3470	150.288	2.132	0.8379	22.6	0.03	43.55	41.72	-0.48	10.77	-0.13	0.65	0.17	44.29	8.36	-2.17	OD
3471	149.959	2.553	1.318	23.62	0.03	43.78	42.42	0.05	10.63	2.06	0.56	0.25	44.92	8.56	-1.74	OD
3472	150.497	2.656	1.2555	24.1	0.04	43.41	42.58	0.03	10.78	0.52	0.65	0.15	43.90	8.34	-2.53	OD
3474	149.864	2.059	1.225	24.11	0.05	43.57	41.75	0.12	10.91	0.22	0.64	0.13	44.71	8.37	-1.75	NL
3475	150.449	1.686	1.405	22.74	0.05	44.11	43.12	-0.51	11.07	2.02	0.76	0.26	45.16	8.80	-1.73	OD
3476	150.365	2.333	1.453	24.82	0.06	43.08		-0.62	10.47	-0.66	0.92	0.10				OD
3480	149.906	2.875	1.236	23	0.08	43.80	42.34	-0.38	11.02	2.26						NL
3481	149.392	2.342	1.127	22.98	0.11	43.84	43.56	-0.16	10.50	2.26						NL
3482	150.422	1.871	1.411	23.87	0.11	43.61	42.70	-0.43	10.87	1.02	0.70	0.11				OD
3483	149.516	2.174	1.306	24.3	0.11	43.31		-0.48	10.86	0.17	0.76	0.14				OD
3484	150.189	2.607	1.0205	22.87	0.15	43.80	42.52	-0.15	10.54	1.63	0.39	0.46	44.77	8.44	-1.76	OD
3485	150.412	1.859	1.24	24.27	0.15	43.40	42.63	-0.22	10.28	0.98	0.96	0.10				OD
3486	150.021	1.791	1.165	23.33	0.17	43.87	43.10	0.04	10.53	1.96	0.71	0.14	44.98	8.61	-1.73	NL
3488	150.243	1.766	0.6227	20.96	0.20	44.19	42.15	-0.15	11.14	0.23	0.64	0.29	45.29	8.63	-1.44	NL
3489	150.538	2.715	1.288	24.05	0.22	43.68	42.45	-0.02	10.73	-0.84	0.91	0.12	44.71	8.31	-1.70	NL
3490	149.570	1.991	0.9997	22.3	0.23	44.13	41.79	-0.14	11.16	0.04	0.74	0.22	45.23	8.49	-1.35	NL
3492	150.200	1.827	0.8952	21.67	0.28	44.25	41.96	-0.37	11.31	1.63	0.93	0.31	45.20	8.97	-1.87	OD
3494	150.158	2.415	0.9	23.39	0.35	43.74	41.68	-0.09	10.90	0.42	0.67	0.28	44.80	8.39	-1.69	OD
3496	149.978	2.398	1.456	23.96	0.40	44.00	42.60	-0.16	10.82	1.85	0.38	0.18	45.06	8.59	-1.63	OD
3498	150.260	2.769	1.308	24.23	0.45	43.80	42.34	-0.12	10.55	1.49	0.61	0.14	44.75	8.40	-1.75	OD
3499	150.163	2.622	1.188	23.78	0.47	43.89	42.31	-0.18	10.53	1.81	0.92	0.10	44.84	8.49	-1.74	NL
3500	150.526	1.829	1.127	23.93	0.48	43.78	42.19	-0.18	10.71	-0.20	0.86	0.10	44.75	8.40	-1.75	NL
3501	150.110	1.725	1.303	24.72	0.49	43.66	42.66	-0.04	10.70	0.01	0.52	0.17				NL
3502	149.818	2.053	1.229	23.81	0.51	44.01	41.69	-0.15	10.58	1.44	0.72	0.15	45.07	8.41	-1.44	NL
3503	150.273	1.934	0.916	22.48	0.51	44.26	43.61	-0.21	11.39	0.06	0.42	0.31	45.31	8.77	-1.56	NL
3504	149.829	2.908	1.414	24.6	0.54	43.93	42.79	0.20	10.94	0.25						NL
3505	150.558	2.261	1.455	23.98	0.60	44.18		-0.24	10.68	2.11	0.98	0.07				OD
3506	149.743	1.952	1.187	23.44	0.64	44.20		-0.34	10.22	2.60	0.86	0.13	45.15	8.77	-1.72	OD
3507	149.656	2.076	1.321	23.99	0.65	44.10	42.34	-0.17	10.80	1.67	0.90	0.10				NL
3508	150.491	2.700	1.0302	22.87	0.72	44.35	42.20	-0.20	10.84	1.59	0.94	0.16	45.36	8.78	-1.51	OD
3508	150.491	2.700	1.0302	22.87	0.72	44.35	42.20	-0.20	10.84	1.59	0.94	0.16	45.36	8.78	-1.51	BL

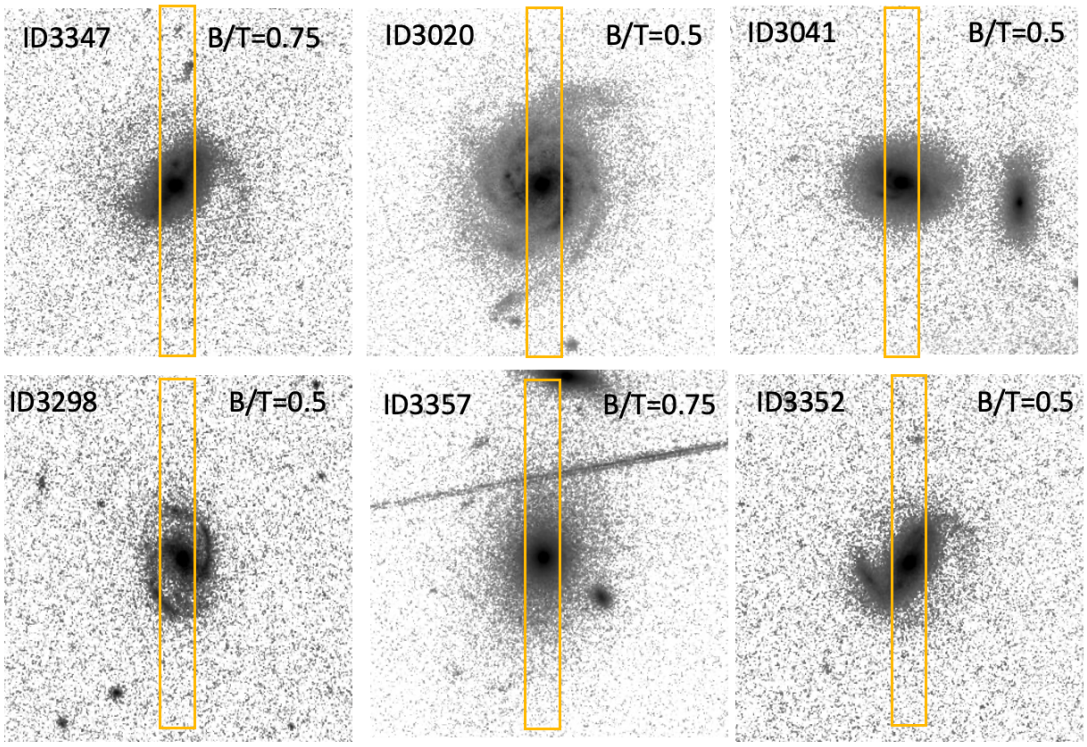

Figure A.1: HST/ACS images of 6 optically dull AGNs. In each $10'' \times 10''$ image, the spectroscopic single slit is overlaid in yellow line ($1.0'' \times 10.0''$). The morphological type of these sample are disk galaxies with different bulge to total ratio which labeled in the upper right at each image.

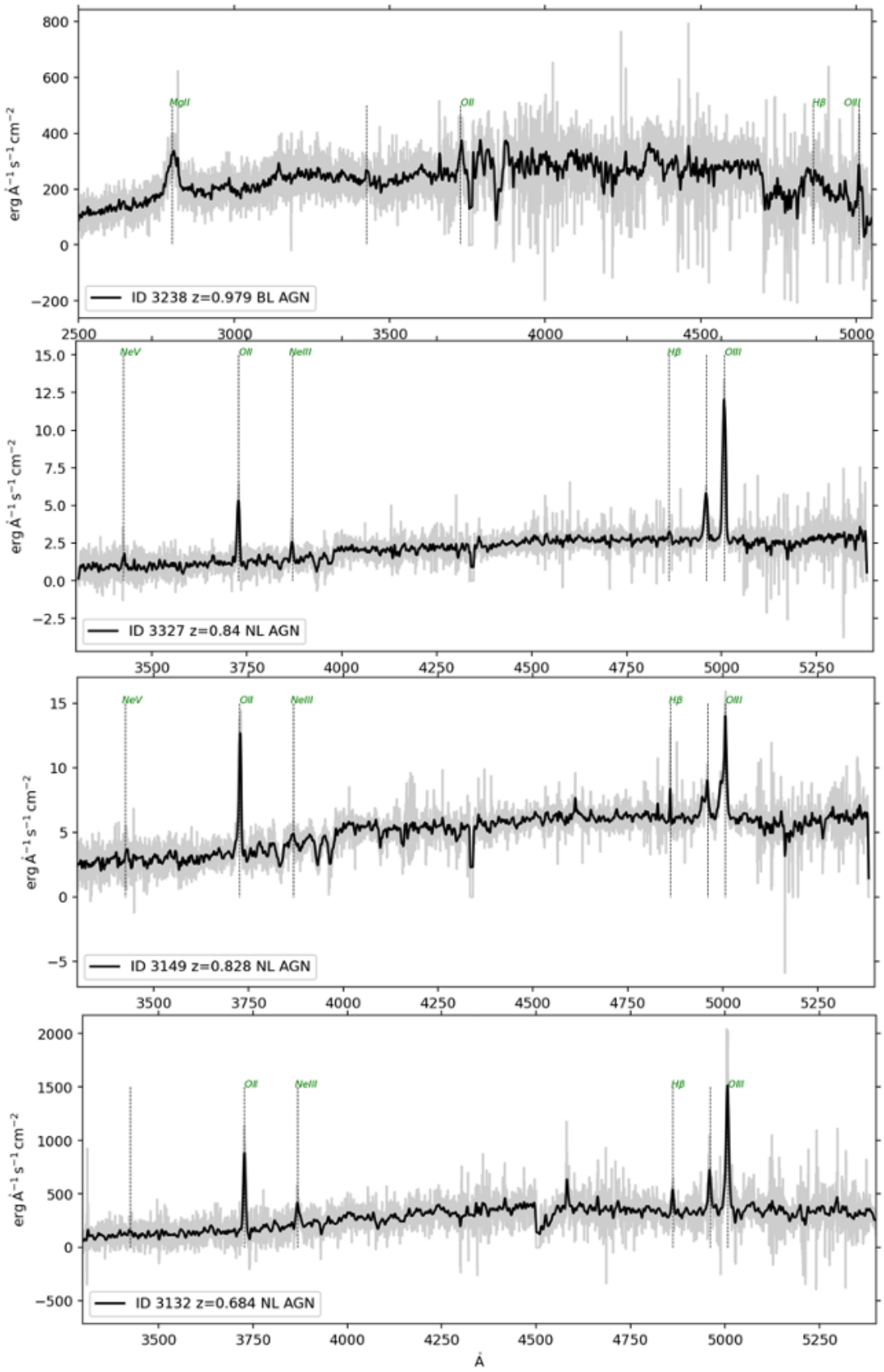

Figure A.2: Spectrum for BL AGN (the upper panel) and the other three spectrum are NL AGN. the ID and redshift for each panel are labeled in the spectrum. All these spectrum are obtained from DEIMOS10K catalog

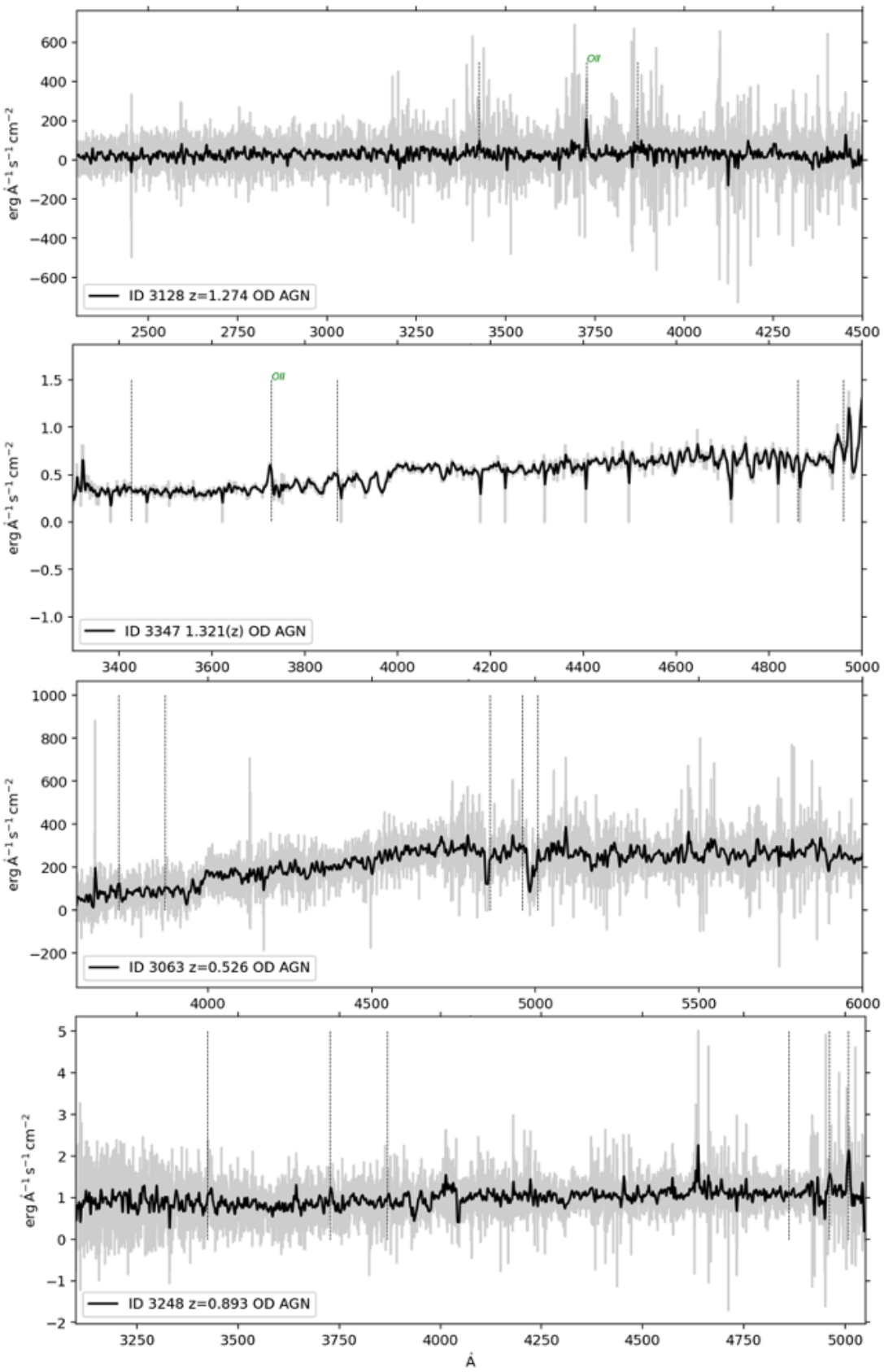

Figure A.3: Spectrum for OD AGN that can't be explained by dilution. All these spectrum are obtained from Deimos10K catalog except for the second spectrum from the top (ID3447) which is obtained from zCOSMOS.